

Title

Phenotypic differences in reversible attachment behavior reveal distinct *P. aeruginosa* surface colonization strategies

Authors

Calvin K. Lee*¹, Jérémy Vachier*², Jaime de Anda ¹, Kun Zhao ³, Amy E. Baker ⁴, Rachel R. Bennett ⁵, Catherine R. Armbruster ^{6,9}, Kimberley A. Lewis ⁴, Rebecca L. Tarnopol ⁷, Charles J. Lomba ¹, Deborah A. Hogan ⁴, Matthew R. Parsek ⁶, George A. O'Toole ⁴, Ramin Golestanian ^{2,8†}, and Gerard C. L. Wong ^{1†}

Affiliations

¹ Department of Bioengineering, Department of Chemistry and Biochemistry, and California NanoSystems Institute, University of California Los Angeles, Los Angeles, CA 90095-1600, USA.

² Max Planck Institute for Dynamics and Self-Organization (MPIDS), Am Fassberg 17, D-37077 Göttingen, Germany.

³ Key Laboratory of Systems Bioengineering (Ministry of Education), School of Chemical Engineering and Technology, Collaborative Innovation Center of Chemical Science and Engineering, Tianjin University, Tianjin 300072, People's Republic of China.

⁴ Department of Microbiology and Immunology, Geisel School of Medicine at Dartmouth, Hanover, NH 03755, USA.

⁵ School of Mathematics, University of Bristol, Bristol BS8 1TW, UK.

⁶ Department of Microbiology, University of Washington, Seattle, Washington 98195, USA.

⁷ Department of Plant and Microbial Biology, University of California Berkeley, Berkeley, CA 94720-3102, USA.

⁸ Rudolf Peierls Centre for Theoretical Physics, University of Oxford, Oxford OX1 3PU, United Kingdom.

⁹ Department of Microbiology and Molecular Genetics, University of Pittsburgh School of Medicine, Pittsburgh, PA, 15219.

† Corresponding authors:

gclwong@seas.ucla.edu

ramin.golestanian@ds.mpg.de

* These authors contributed equally to this work.

Abstract

Despite possessing the machinery to sense, adhere to, and proliferate on surfaces, it is commonly observed that bacteria initially have a difficult time attaching to a surface. Before forming a bacterial biofilm, planktonic bacteria exhibit a random period of transient surface attachment known as “reversible attachment” which is poorly understood. Using community tracking methods at single-cell resolution, we examine how reversible attachment progresses during initial stages of surface sensing. *Pseudomonas aeruginosa* strains PAO1 and PA14, which exhibit similar exponential trends of surface cell population increase, show unanticipated differences when the behavior of each cell was considered at the full lineage level and interpreted using the unifying quantitative framework of an exactly solvable stochastic model. Reversible attachment comprises two regimes of behavior, processive and nonprocessive, corresponding to whether cells of the lineage stay on the surface long enough to divide, or not, before detaching. Stark differences between PAO1 and PA14 in the processive regime of reversible attachment suggest the existence of two complementary surface

38 colonization strategies, which are roughly analogous to “immediate-” vs “deferred-gratification” in a prototypical
39 cognitive-affective processing system. PAO1 lineages commit relatively quickly to a surface compared to PA14 lineages.
40 PA14 lineages allow detaching cells to retain memory of the surface so that they are primed for improved subsequent
41 surface attachment. In fact, it is possible to identify motility suppression events in PA14 lineages in the process of
42 surface commitment. We hypothesize that these contrasting strategies are rooted in downstream differences between
43 Wsp-based and Pil-Chp-based surface sensing systems.

44 Keywords

45 Bacteria biofilms | *Pseudomonas aeruginosa* | Reversible attachment | Stochastic model | Surface sensing

46 Importance

47 The initial pivotal phase of bacterial biofilm formation known as “reversible attachment,” where cells undergo a period
48 of transient surface attachment, is at once universal and poorly understood. What is more, although we know that
49 reversible attachment culminates ultimately in irreversible attachment, it is not clear how reversible attachment
50 progresses phenotypically as bacterial surface sensing circuits fundamentally alters cellular behavior. We analyze diverse
51 observed bacterial behavior one family at a time (defined as a full lineage of cells related to one another by division)
52 using a unifying stochastic model and show that it leads to new insights on the time evolution of reversible attachment.
53 Our results unify apparently disparate findings in the literature regarding early events in biofilm formation by PAO1 and
54 PA14 strains.

55 Introduction

56 Biofilms are surface-adhered communities or suspended aggregates of bacteria that have increased tolerance to
57 environmental stresses and antibiotics, and impact human health and the environment in complex ways. These biofilms
58 can be harmful by causing diseases (1, 2), and can be beneficial by serving as commensals in various hosts as well as
59 having applications in bioremediation and energy production (3). A critical step in forming a bacterial biofilm is surface
60 sensing (4), where free-swimming planktonic cells detect, attach to, and physiologically respond to a surface. Recent
61 work has shown that different appendages or extracellular structures, such as flagella (5, 6) or type IV pili (TFP) (7, 8) are
62 involved in activating cellular responses (e.g., protein production, motility, and biofilm formation) during surface
63 sensing. In many bacterial species, these responses are primarily controlled by intracellular secondary messenger
64 molecules, such as cyclic diguanylate (c-di-GMP) (9-16) and cyclic AMP (cAMP) (8, 17, 18). For the case of *Pseudomonas*
65 *aeruginosa*, a clinically relevant model system (19), there are at least two well-studied but distinct surface sensing
66 circuits, the Wsp and the Pil-Chp systems, that can contribute to initiating biofilm formation. In our current
67 understanding, the Wsp system senses through the membrane-bound, chemosensory-like Wsp protein complex which
68 localizes laterally along the cell body (10), activating the diguanylate cyclases WspR and c-di-GMP synthesis via a
69 mechanism that requires clustering of (20). On the other hand, the Pil-Chp system senses a surface through polarly-
70 localized TFP, which activates the adenylate cyclases CyaB and results in cAMP synthesis. Increased cAMP levels then
71 induces the production and secretion of PilY1, which in turn activate the diguanylate cyclases SadC and results in c-di-
72 GMP synthesis (17). Downstream consequences of c-di-GMP synthesis include exopolysaccharide (EPS) production and
73 motility suppression. Different strains of *P. aeruginosa*, such as PAO1 and PA14, utilize these surface sensing
74 mechanisms to varying extents. The PAO1 strain predominantly uses the Wsp system (21) leading to the surface
75 deposition of the EPS Psl (22, 23), while PA14 predominantly uses the Pil-Chp system leading to the suppression of
76 surface motility (17) and production of a Pel-dominant biofilm matrix (24).

77 Despite the existence of diverse machinery to sense, adhere to, and proliferate on surfaces, it is commonly observed
78 that bacteria initially seem to have a difficult time attaching to a surface, as indicated by typical flow cell studies where
79 *P. aeruginosa* often takes >20 h before attaching to the surface in large numbers (25, 26). This phenomenon was first
80 reports in the 1930s (27, 28). Using high speed microscopy to measure the distribution of surface residence times, it was
81 previously observed that the overwhelming majority of cells that land on the surface eventually detach, and it is only
82 after a prolonged and variable time lag that cells begin to rapidly cover the surface (8). Reversible attachment is

counterintuitive and difficult to understand for a number of reasons. We stress that the low apparent probability of successful attachment is not simply a matter of cells “bouncing” off the surface. (During reversible attachment, it is not uncommon for cells to attach and stay long enough to divide but then subsequently detach.) Moreover, the unpredictability of reversible attachment cannot be circumvented with better measurement statistics: the duration of reversible attachment always appears random and do not converge to a specific duration for the same initial conditions. This combination of characteristics in reversible attachment, low probability of success, intrinsic time dependence, and structurally random outcomes, suggests that use of a stochastic model may lead to new understanding. From a foundational perspective of surface sensing, although we know that reversible attachment can culminate in irreversible attachment, it is not clear how reversible attachment progresses phenotypically as bacterial surface sensing circuits fundamentally alters cellular behavior, and ultimately improve on an initial attachment probability of effectively zero.

Here, we show that the use of an exactly solvable “divide-detach” stochastic model, designed to examine the reversible attachment behaviors of *P. aeruginosa* PAO1 and PA14 lineages in the form of family trees, reveals differences in their biofilm formation behavior during reversible attachment. Within this model, reversible attachment is described by two parameters: effective division rate and effective detachment rate. We find that reversible attachment can be understood if we analyze behavior using lineage time (the time a lineage stays continually on the surface) rather than an experiment time, defined by time from inoculation. Specifically, reversible attachment comprises two regimes of behavior, defined by whether cells of the lineage stay on the surface long enough to divide, or not, before detaching. For lineages that detach before dividing at all, both PAO1 and PA14 behave similarly with near certain lineage “extinction,” wherein the entire lineage detaches. For lineages that stay long enough to divide, PAO1 and PA14 show surprisingly different behaviors. Our theoretical model provides a framework wherein time-dependent division and detachment rates and distributions of lineages can be extracted from our experiments. Our results suggest that PAO1 and PA14 utilize two fundamentally different surface colonization strategies. For PAO1, individual lineages commit relatively quickly to a surface compared to PA14, resulting in a steady progressive increase of a surface cell population that is irreversibly attached (i.e., committed to forming a biofilm). In contrast, PA14 lineages have high rates of cell detachment from surfaces. However, these detaching cells retain a memory of the surface (8), and ultimately form a planktonic population that is primed for attachment, so that sudden increases in irreversibly attached surface cell populations can occur. Our model provides a framework for categorizing different surface colonization strategies that lead to biofilm formation, and it is conceivable that in principle each approach has its own advantages under different circumstances.

Results

Two regimes of reversible attachment in PAO1 and PA14 are revealed through lineage analysis

When monitoring the number of cells on the surface as a function of the time from inoculation of the flow cell (denoted as experiment time), both strains follow a similar pattern (Figure 1). At early times, widespread detachment behavior is observed. Despite both division and additional attachment, the surface population essentially remains constant for a long and variable lag period (~10-20 h), after which the surface population will then begin to rise steeply, in a manner that can be fit to an exponential growth curve. However, further distinguishing their behaviors in a finer pitch of detail is difficult due to the random nature of reversible attachment. When comparing the surface population increases between PAO1 and PA14, we observe nearly all possibilities: we either observe that PAO1 has a steeper and earlier rise in the surface population compared to PA14, that PAO1 and PA14 have similar rises, or that PA14 has an earlier and steeper rise than PAO1 (Figure S1). Furthermore, it is difficult to correlate these observations with macroscopic crystal violet biofilm assays, where PAO1 has statistically significantly higher OD_{550nm} values compared to PA14 (Figure S2), which suggests that PAO1 is capable of forming early biofilms faster than PA14. PAO1 has a mean $OD_{550nm} = 0.23$ with a 95% confidence interval of (0.19, 0.26), while PA14 has a mean $OD_{550nm} = 0.14$ with a 95% confidence interval of (0.099, 0.18). Comparing the bootstrap sampling distributions of the mean OD_{550nm} values (which also generate the 95% confidence intervals) show that PAO1 has a higher mean OD_{550nm} value than PA14 (p-value of 0.0002). Using the median instead of the mean gives similar results. PAO1 has a median $OD_{550nm} = 0.22$ with a 95% confidence interval of (0.17, 0.29), while PA14 has a median $OD_{550nm} = 0.12$ with a 95% confidence interval of (0.094, 0.21). Comparing the bootstrap sampling distributions of the median OD_{550nm} values (which also generate the 95% confidence intervals)

130 show that PAO1 has a higher median OD_{550nm} value than PA14 (p-value of 0.003). These apparently conflicting
131 observations are not easily resolved with increased data collection since they arise from the intrinsic randomness of the
132 process and not from incurring measurement errors. This intrinsic randomness, which is not uncommon in different
133 aspects of biofilm formation, is usually neglected in analyses. In the present context, these effects complicate any
134 analysis of the reversible attachment behaviors in PAO1 and PA14, that depend on traditional methods to monitor the
135 number of surface cells as a function of experiment time or by macroscopic assays.

136 To account for the random nature of reversible attachment and the large fluctuations in the observations, we
137 investigate the evolution of bacterial behavior as a function of surface sensing progression using lineage analysis. We
138 monitor the time that a given isolated family, consisting of an attached cell (founder cell) and its progeny (daughter
139 cells) via division, stays continually on the surface, which we designate as lineage time ($t = t_{lineage}$). For each family,
140 we begin tracking at the frame that an individual, founder bacterium attaches and assign this time as $t_{lineage} = 0$ h. We
141 continue tracking until either the entire family detaches, or until we lose track of that family (where we can no longer
142 distinguish individual cells, or the cells move out of the recording boundaries). This final time point is recorded as the
143 family's residence time. During reversible attachment regimes, families are categorized by whether a division event
144 occurs or not before detaching. We denote families that detach before dividing at all as the "nonprocessive" regime of
145 reversible attachment, and families that divide one or more times before detaching as the "processive" regime of
146 reversible attachment, using language from enzyme kinetics. It is important to note that these regimes are distinct from
147 irreversible attachment because during both regimes of reversible attachment, detachment is still prominent, while
148 during irreversible attachment, detachment is much less common. All families analyzed here are shown in Figure 2 and
149 Figure S3.

150 Cells in both nonprocessive and processive regimes are present throughout the entire biofilm formation process.
151 However, during the initial variable lag period, where the total surface population is not increasing, almost all cells are in
152 the nonprocessive regime, while very few cells are in the processive regime. As experiment time elapses, the general
153 observed trend is that cells in the processive regime become more common, while cells in the nonprocessive regime
154 become less common, especially during period of surface population exponential increase. However, it is difficult to
155 quantify such cellular behavior in this system because both regimes coexist with fluctuating proportions due to the
156 inherent randomness in single cell behavior, thereby complicating any analysis of biofilm behavior as a function of
157 experiment time. Thus, we utilize an analysis of lineage time to quantify the behavior of individual families in each
158 regime.

159 When comparing the two regimes for either PAO1 or PA14, we find that the residence times are drastically different. In
160 the nonprocessive regime, ~99% of cells stay on the surface for less than 30s for both strains. Furthermore, of the
161 ~20,000 tracked families in the nonprocessive regime (both PAO1 and PA14), we observe less than 10 families (~0.05%)
162 that have residence times comparable to the average doubling time of 1-2 h (Figure S4), which is the minimum residence
163 time for families in the processive regime. Detachment dominates attachment and division in the nonprocessive regime,
164 and essentially the surface population does not increase over the first 10-20 h of experiment time. In contrast, cells in
165 the processive regime are in continuous contact with the surface for longer periods of time. Moreover, virtually all of the
166 cells that remain surface engaged in the processive regime do so longer than cells in the nonprocessive regime. Finally,
167 cells in the processive regime grow and divide on the surface and have clearly altered their behavior compared to
168 "surface-naïve" planktonic cells, presumably as a consequence of activating surface sensing pathways.

169 Interesting trends emerge when comparing PAO1 and PA14 lineages in each regime. In the nonprocessive regime, we
170 find that PAO1 and PA14 exhibit similar behaviors, where cells experience the surface transiently. However, in the
171 processive regime, we see stark differences between PAO1 (44 families with 622 total descendants analyzed) and PA14
172 (31 families with 381 total descendants analyzed) (Figure S3). PAO1 families have more progeny retained on the surface,
173 while PA14 families have more progeny detaching, which can be seen in a broad range of metrics. For example, we can
174 compare single cell detachment behavior via the proportion of detachment vs division events. PAO1 has a statistically
175 significantly lower proportion, with 143 (33%) detachment vs 289 (67%) division events, compared to PA14, with 130
176 (43%) detachment vs 175 (57%) division events, according to the χ^2 test (p-value of 0.008). We can compare family-

177 averaged detachment behavior with family tree asymmetry parameter Λ (8). Λ values closer to zero indicate a more
178 symmetric family tree where more progeny are retained (more “two-legged” division nodes in the family tree, where
179 both post-division daughter cells stay on the surface), while Λ values closer to one indicate a more asymmetric family
180 tree where more progeny detach (more “one-legged” division nodes in the family tree, where one of the post-division
181 daughter cells detach from the surface). PAO1 family trees have a median $\Lambda = 0.33$ with a 95% confidence interval of
182 (0.25, 0.39), while PA14 family trees have a median $\Lambda = 0.42$ with a 95% confidence interval of (0.37, 0.52). Comparing
183 the bootstrap sampling distributions of the median tree asymmetry values (which also generate the 95% confidence
184 intervals) show that PAO1 family trees have a lower median Λ than PA14 family trees (p-value of 0.015). Overall, our
185 data show that PAO1 and PA14 display similar behaviors during the nonprocessive regime, but during the processive
186 regime, PAO1 shows a significantly higher likelihood of remaining surface-associated.

187 “Divide-detach” stochastic model highlights differences between PAO1 and PA14 in the processive 188 regime of reversible attachment

189 Our observations suggest that PAO1 is less prone to detachment than PA14. However, these metrics do not properly
190 consider the collective time-dependent effects of division and detachment. For example, having more detachment
191 events earlier in lineage time would have a much greater effect on the resulting family architecture compared to the
192 same detachment events occurring several generations later. Even at the single cell level, gene expression is stochastic
193 and can occur in a burst-like, intermittent manner (29), which contributes additional randomness to that cell’s behavior.
194 Consequently, the behavior of an individual bacterium (in terms of whether or not in every instance they stay on the
195 surface or detach after a division event) may be completely random and can only be described using statistical metrics.
196 Since biofilm formation can be seen as an evolution of a population of random individual bacteria, it can be described as
197 a stochastic process that depends on a number of control parameters as well as random environment variables.
198 Consistent with that contention, large fluctuations are often observed in measured parameters (e.g., family trees), and
199 these fluctuations are not easily mitigated with increased data collection since they arise from the intrinsic randomness
200 of the process and not from incurring measurement errors. In general, although it is acknowledged that the
201 unpredictability of single cell behavior can be important to surface sensing and biofilm development, this randomness is
202 rarely accounted for in traditional microbiological studies.

203 To obtain more time-dependent comparisons that incorporate division and detachment effects, and to help account for
204 the inherent randomness in observed family trees, we develop a “divide-detach” stochastic model. We use this model to
205 study the temporal evolution of the expected number of surface cells in a family tree, or population size (30-35). In this
206 model, the population size can increase or decrease by one bacterium as time evolves, and the population size can be
207 infinite or null. The corresponding sample space Ω is given by $\Omega = \{0, 1, 2, \dots, N, \dots\}^m$, where m is the number of
208 independent family trees, or different populations of bacteria. As time evolves, the population size can change and
209 result in a sequence $\omega \in \Omega$, where ω is the set of family trees that are in the experiment. For example, if there is $m = 1$
210 family tree, then $\omega = \{\omega_1\}$, and if there are m family trees, then $\omega = \{\omega_1, \dots, \omega_m\}$. However, because this is a
211 stochastic process, we cannot predict ahead of time what ω will be. Instead, what we know for ω are the set of possible
212 observations (states) Σ and the actual observations X_t from experiments. The set of states is given by $\Sigma =$
213 $\{0, 1, \dots, N, \dots\}$, where N represents the number of surface cells in a family and is infinite. Σ tells us what observations
214 (number of surface cells) are possible for any family tree during an experiment. The actual observations of ω are given
215 by $X_t(\omega) = \{X_t^1(\omega_1), X_t^2(\omega_2), \dots, X_t^m(\omega_m)\}$, which is how many surface cells are observed in each of the m family trees
216 at time point t during an experiment, and $X_t(\omega)$ is a random variable $X_t: \omega \rightarrow \Sigma$ that defines this stochastic process.
217 Having a random variable means that for the family trees ω and each time point t , we observe $X_t(\omega)$ taken from the set
218 of states Σ according to a certain (not necessarily known) probability distribution; but when we repeat the experiment,
219 we will not necessarily observe the same $X_t(\omega)$ for the same time point t and family trees ω . Figure 3 shows examples
220 of this process for $m = 1$ family tree (Figure 3a) and for $m = 3$ family trees (Figure 3b).

221 The dynamics of such a stochastic process are given by the evolution of the probability distribution $P(j, s + t | i, s)$, which
222 gives the probability of transitions between all states for all $t \geq 0$ and can be rewritten as $P_t(j | i)$. For a family tree, the
223 only possible transitions are the neighboring transitions, $n \rightarrow n + 1 = (n + 1 | n) = \lambda_n$ and $n \rightarrow n - 1 = (n - 1 | n) =$

224 μ_n . As a result, the dynamics of this process can be described by looking only at the evolution of the probability
225 distribution $P_t(n|n)$ for state $n \in \Sigma$. The rates λ_n and μ_n determine the intensity of increase (i.e., division) or decrease
226 (i.e., detachment), respectively, for state n . In a family tree, each cell can divide (with a division rate λ) or detach (with a
227 detachment rate μ), so the rates become $\lambda_n = \lambda n$ and $\mu_n = \mu n$. Figure 3c shows a schematic of the dynamics described
228 here (i.e., how the population size can increase or decrease).

229 The equation describing the evolution of this process is given by the Kolmogorov backward equation, also called the
230 master equation, which reads

$$\frac{dP_0}{dt} = \mu P_1, \quad n = 0$$

and

1

$$\frac{dP_n}{dt} = (\mu)(n+1)P_{n+1} - (\lambda + \mu)(n)P_n + (\lambda)(n-1)P_{n-1}, \quad n > 0,$$

231 where $P_n = P_n(t) = P_t(n|n)$, $P_{n+1} = P_{n+1}(t) = P_t(n+1|n)$, and $P_{n-1} = P_{n-1}(t) = P_t(n-1|n)$. We refer the readers
232 to the methods to find the details of the solution to this equation.

233 Experimentally, by having access to m independent family trees, it is possible to build the probability distribution by
234 counting the number of families that have zero cells, one cell, two cells, and so on, at a given lineage time t . In other
235 words, for each time point t , we plot the actual observations $X_t(\omega)$ on a histogram to derive the probability of each of
236 the states n occurring. For families in the processive regime of reversible attachment, we avoid potential problems
237 arising from tracking limitations by selecting $m = 11$ families for PAO1 (out of 44 families) and $m = 12$ families for PA14
238 (out of 31 families), with a t_{lineage} range of 0-12 h for PAO1 and 0-10 h for PA14 (see Figure S3 caption for family
239 selection criteria).

240 Comparing the experimental data with the model is not straightforward when using the probability distributions
241 directly. In the experimental data, there are a finite number of families and a finite number of cells in a family, which
242 means that it is difficult to generate distributions that are well populated for quantitative comparisons. To overcome this
243 limitation, we employ the method of moments, which provides information about the distributions, to fit the model to
244 experimental data and obtain the rates. Instead of comparing the experimental and model probability distributions
245 $P_n(t)$, we compare the experimental and model moments, $\langle n(t)^k \rangle$, where k is the k -th moment. We can calculate the
246 experimental moments directly from the experimental probability distribution, and we can obtain the model moments
247 from the model probability distribution (eq. 2) given by the master equation (eq. 1). The equations for the model
248 moments are shown in the methods (eq. 3-4). To compare experiment with model, we use the first two moments. The
249 first moment is the mean, and the second moment is related to the variance, since the variance equals the second
250 moment minus the first moment squared.

251 When we plot the moments calculated from the experimental data for families in the processive regime of reversible
252 attachment (Figure 4), striking differences between PAO1 and PA14 are revealed. PAO1 follows an exponential growth
253 curve, while PA14 follows a Gaussian curve. These curves are consistent with what we see in the family trees. For PAO1,
254 many of the families have increasing number of cells, while for PA14, fewer of these families are present, and most
255 families end in detachment. However, as we have previously shown, PA14 cells that detach have already initiated the
256 surface sensing process, and they retain memory of the surface based on their prior surface residence, which primes
257 them for subsequent irreversible attachment (8). Also, from our data, the variances for both PAO1 and PA14 can be as
258 large as the mean population size, indicating that extinction in an individual lineage can happen at any time, even in a
259 population that is exponentially growing on average. Therefore, it is important to note that individual lineage
260 “extinction” events (where the entire family detaches) do not indicate a failure to form a biofilm.

261 With our model, the temporal evolution of a family tree can be described by the single cell division (λ) and detachment
262 (μ) rates. λ is likely related to cellular events that contribute to surface growth, which can be affected by complex
263 factors such as changes in cellular metabolism or the local availability of nutrients. Likewise, μ is likely to be related to

264 cellular events that contribute to detachment, such as the production of EPS and the activities of motility appendages.
265 Both rates can be time-dependent in principle, so $\lambda = \lambda(t)$ and $\mu = \mu(t)$. For example, as bacteria continue
266 proliferating on the surface, they can spend more of their metabolic energy towards EPS production rather than for
267 division, and they can start detaching less. However, finding the exact functional form of time dependence to use in the
268 model is difficult. We first start with the simplest form of time-dependence (linear, or first order polynomial), where
269 $\lambda(t) = L_0 + L_1 t$, $\mu(t) = C_0 + C_1 t$, and $\{L_0, L_1, C_0, C_1\}$ are the coefficients that we obtain by fitting the experimental
270 data to the model. $\lambda(t)$ and $\mu(t)$ are rates that represent probabilities per time unit, which means they are positive and
271 have dimensions of inverse time, $[\lambda] = [\mu] = [\text{time}]^{-1}$. Therefore, the coefficients L_0 and C_0 also have dimensions
272 $[L_0] = [C_0] = [\text{time}]^{-1}$, and the coefficients L_1 and C_1 have dimensions $[L_1] = [C_1] = [\text{time}]^{-2}$. By dimensional
273 analysis, we can extract time scales for lineage-level growth (via division) and death (via detachment) behaviors from
274 either the rates (λ^{-1} and μ^{-1}) and the coefficients (L_0/L_1 and C_0/C_1). If the experimental data and model do not show
275 good agreement, then we can reiterate this process with progressively more complicated functions. Additionally, the
276 shape of the experimental moments can guide us in choosing the correct function for the rates.

277 With linear time dependence, we already obtain good agreement when fitting using nonlinear least-squares, as shown
278 by the results of the model fits to the experimental moments in Figure 4. To ensure the fit results give meaningful
279 coefficient values, we set the following constraints based on experimental data. The rates are positive, so $\lambda(t) > 0$ and
280 $\mu(t) > 0$. As seen in the family trees in Figure 2 and Figure S3, division events are roughly evenly spaced out in time, and
281 cells are not nutrient-limited inside the experimental system, so $\lambda(t)$ should be constant. Thus, we set $L_1 = 0$, and
282 $\lambda(t) = L_0$. We consider any coefficient $< 10^{-5}$ as zero for subsequent analysis based on the precision of the
283 experimental data. The resulting coefficients from the fits are as follows: for PAO1, $L_0 = 0.136 \text{ h}^{-1}$, $L_1 = 0 \text{ h}^{-2}$, $C_0 =$
284 0.0242 h^{-1} , $C_1 = 0.00147 \text{ h}^{-2}$, and for PA14, $L_0 = 0.256 \text{ h}^{-1}$, $L_1 = 0 \text{ h}^{-2}$, $C_0 = 0 \text{ h}^{-1}$, $C_1 = 0.107 \text{ h}^{-2}$.

285 We find that $\mu(t)$ is time-dependent for both strains (i.e., C_1 is non-zero). For PAO1, we find that μ is slowly increasing,
286 since C_1 is ~ 1 order of magnitude smaller than C_0 , and both coefficients are positive and smaller than L_0 . For PA14, μ is
287 increasing quite rapidly, since C_1 is positive and is much greater than C_0 . Because $\mu(t)$ is time-dependent, the relevant
288 time scale τ_μ to extract for time-dependent lineage-level detachment behavior for both PAO1 and PA14 is $\tau_\mu = C_0/C_1$
289 ($\approx 16 \text{ h}$ for PAO1, and 0 h for PA14). Also, because $\lambda(t)$ is constant, the relevant time scale τ_λ to extract for time-
290 independent lineage-level division behavior for both PAO1 and PA14 is $\tau_\lambda = L_0^{-1}$ ($\approx 7 \text{ h}$ for PAO1, and $\approx 4 \text{ h}$ for PA14).
291 These values are consistent with the experimental data. Interestingly, for both strains, we find that τ_λ is bigger than the
292 average division time by a factor of ~ 3 , which means that τ_λ corresponds to ~ 3 generations of division. The value of τ_λ
293 corresponds closely to the time that a given lineage persists on the surface before ultimately going extinct and detaching
294 (i.e., residence time). To calculate the mean residence times of the experimental lineages in Figure 2, we only include
295 lineages that ultimately detach before the cutoff time (12 h for PAO1, 10 h for PA14). This results in $\approx 6 \text{ h}$ for PAO1 and
296 $\approx 5 \text{ h}$ for PA14, which are very close to the τ_λ values obtained from the coefficients ($\approx 7 \text{ h}$ for PAO1, and $\approx 4 \text{ h}$ for PA14,
297 see above). For PAO1, having a larger τ_λ and a slowly increasing and relatively small μ mean that lineages are division-
298 dominant ($\lambda > \mu$) as they spend more time on the surface. Rather than ultimately detaching, we see many lineages
299 persist on the surface and increase their number of cells despite having detachment events. At $t_{\text{lineage}} = 12 \text{ h}$, 7 of the
300 11 families still exist on the surface (Figure 2c, #1-7). For PA14, having a smaller τ_λ and a rapidly increasing μ means that
301 lineages are initially division-dominant ($\lambda > \mu$), but then become detachment-dominant ($\mu > \lambda$) after a certain amount
302 of time on the surface, which is also the time scale described by τ_λ . We see that many lineages grow to at least 2-3
303 generations, which corresponds to the lineage time where $\lambda > \mu$. Once $\mu > \lambda$, then many families begin to detach until,
304 at $t_{\text{lineage}} = 10 \text{ h}$, only 1 of the 12 families still exists on the surface (Figure 2d, #1). Clearly, unlike PAO1, PA14 cells that
305 have started the surface sensing process do not necessarily stay on the surface. Rather, as we have shown previously (8),
306 they rejoin the planktonic population as “surface-sentient” cells that are primed for longer surface residence times
307 during subsequent attachment. Similarly, the value of τ_μ corresponds closely to cellular activities that affect
308 detachment, such as, for example, the competition between EPS production and motility appendage activity. EPS is
309 likely to affect detachment more for PAO1 than for PA14, since PAO1 is known to produce the Psl EPS, while PA14
310 cannot. On the other hand, presumably because of the Pil-Chp system, motility appendage activity is likely to affect

311 detachment more for PA14 than for PAO1. Consistent with this hypothesis, PAO1 has a much larger τ_{μ} compared to
312 PA14 (which is zero).

313 With these model parameters, we can evaluate the model probability distribution $P_n(t)$ to then compare with the
314 experimental probability distribution $P_n(t)$. We show the comparisons of the probability distributions with two different
315 visual representations in Figure 5. The first is plotting $P_n(t)$ vs n for specific lineage times $t = \{2.5, 5, 7.5, 10\}$ h, and the
316 second is plotting the entire $P_n(t)$ vs n and t as a contour plot. The plots of the probability distributions also show good
317 agreement. For the probability contour plots, agreement between experiment and model are assessed as follows. The
318 regions of high ($P_n(t) \sim 1$) and low ($P_n(t) \leq 10^{-2}$) probability contours are similar in shape and location (in the n, t
319 plot space) between experiment and model. The shapes of the probability contours are consistent with the plots of the
320 moments in Figure 4. For PAO1, as t progresses, the probability of having more cells per family (higher n) increases. For
321 PA14, the probability of having higher n increases and then decreases as t progresses. However, further direct
322 comparisons of the probability distributions are difficult. As previously mentioned, the experimental probability
323 distributions will invariably be sparser than the model probability distributions, which can be seen in the plots as either
324 jagged lines or holes in the contours. This sparseness comes from having finite experimental data and is not
325 straightforward to remove (e.g., via interpolation). Nevertheless, the model probability distribution can be used to
326 describe what family tree architectures we expect to observe during similar experiments.

327 The model can also be applied for cells in the nonprocessive regime of reversible attachment. We find that for both
328 PAO1 and PA14, the moments fit to an exponential decay function (Figure 6). This is what the model predicts if there is
329 only detachment and no division, and it correctly describes the data, because cells in the nonprocessive regime detach
330 before dividing on the surface. Furthermore, the variances are of the same order of magnitude as the mean population,
331 which means that lineages can become extinct at any time. Thus, for both processive and nonprocessive regimes of
332 reversible attachment, the stochastic model described here accurately describes the behaviors of PAO1 and PA14,
333 including their differential paths to irreversible attachment.

334 PAO1 and PA14 have distinct progressions of surface colonization, which suggest contrasting surface 335 engagement strategies

336 Our observations and results imply that both PAO1 and PA14 start their initial surface engagement with similar behavior
337 (in terms of surface residence times) in the nonprocessive regime of reversible attachment, but then they diverge
338 strongly in the processive regime of reversible attachment. PAO1 shows an increase in the number of families that
339 commit relatively quickly to surface growth, and this is likely a factor that contributes to the trend of PAO1 forming
340 faster biofilms compared to PA14 as seen in the crystal violet assays (Figure S2). For PAO1, this early attachment
341 behavior can be more intuitive when correlating with the general progression of biofilm formation. PA14, in contrast,
342 shows a larger number of detachment-dominated families even though the entire population eventually forms a biofilm,
343 which can be a counterintuitive result. Compared to PAO1, where production of sticky EPS appears to be the dominant
344 mechanism driving irreversible attachment (22, 23), PA14 appears to utilize a different surface colonization strategy
345 dependent on progressive suppression of surface motility appendage activity (8), but it is not obvious is how this motility
346 suppression strategy can lead to rapid changes in bacteria detachment rates from surfaces, as shown by the model.

347 We investigated how detachment events occur for PA14 to gain insight into this alternate surface colonization strategy
348 and why appendages and their activities can give rise to a time-dependent detachment rate μ . Consistent with previous
349 results where flagellum-mediated surface spinning generally results in a detachment event (36), we find that ~90% of
350 detachment events occur when a cell has the mature flagellum inherited from its ancestor, as opposed to that cell
351 having to form a new flagellum post-division (Figure 7a,c). Interestingly, deleting the *pilA* gene ($\Delta pilA$, missing the major
352 subunit of the TFP filament) results in significantly fewer detachment events (χ^2 test p-value $\ll 10^{-4}$) for cells that have
353 a mature flagellum. Compared to WT, only roughly half of detachment events occur when the cell has a mature
354 flagellum in the $\Delta pilA$ mutant (Figure 7b,c), an observation that suggests that TFP are important to the detachment
355 process. For the $\Delta pilA$ mutant (and to a much lesser extent in WT), we also observe detachment events with cells that
356 did not have a labeled flagellum, which suggests that non-flagellum-mediated detachment events can also occur.

357 To study how TFP can influence flagellum-mediated spinning and detachment, we adapt a previously developed
358 hydrodynamic model (37). Simulations show that TFP activity (i.e., extension or retraction) can lead to changes in the
359 cell body tilt angle relative to the surface. In the case where the non-flagellated pole is attached to the surface, TFP
360 extension during flagellum-mediated spinning results in the cell tilting to near vertical orientations, while retraction
361 results in a smaller tilt angle (Figure 7d). During flagellum-mediated spinning, near vertical orientations correlate with
362 higher rates of detachment, while orientations closer to the surface correlate with a decreased likelihood of detachment
363 (36, 38). Consistent with previous results, the cell without TFP is more likely to assume an orientation closer to the
364 surface (i.e., horizontal), while the cell with TFP extended the entire time is more likely to assume a near vertical
365 orientation (8).

366 These results suggest that detachment rates are higher when TFP activity and flagellum activity are high and/or coincide,
367 and that detachment rates are lower when the activities are reduced and/or do not coincide. Given that PA14 has small
368 average family size, small surface residence times, and large surface detachment rates, observations of suppression of
369 both appendage activity and detachment are expected to be extremely rare during reversible attachment (i.e., while
370 cells are transiently on the surface). Nevertheless, in our family tree data, we can find examples where we can compare
371 cells from the same generation but on different branches of the family tree. In these cases, we observe detachment in
372 branches where appendage activities are high (and/or coincide), and no detachment in branches where appendage
373 activities are reduced and/or do not coincide (Figure 8). In example (i), we see that appendage activity is reduced around
374 $t_{\text{lineage}} \sim 6$ h, which coincides with the presence of a division event where no daughter cells detach. In examples (ii) and
375 (iii), appendage activity does not become quiescent and detachment continues to occur for subsequent division events.
376 This appendage activity analysis was repeated with $\Delta pilA$ for validation and was consistent with previous results (Figure
377 S5).

378 Discussion

379 Clearly, the application of stochastic models can be quite powerful in understanding microbiological systems that involve
380 strong fluctuations. The behavior of each lineage is a record of how a specific cell and its progeny managed to stay and
381 proliferate on the surface during cellular changes induced by surface sensing, which has multigenerational
382 consequences. Even though the probability of a specific cell attaching to a surface and proliferating successfully is
383 initially vanishingly small, surface sensing can modify outcomes by changing the structure of family trees, as we can see
384 from the evolution of reversible attachment from the nonprocessive to processive regimes, for example. Interestingly,
385 that the process of reversible attachment can be described by a stochastic model is telling: whether a bacterium
386 encountering a surface makes it to irreversible attachment and eventually participates in biofilm formation may be
387 quantitatively cognate to the description of whether patient zero's disease will die out after a few infections, or take
388 hold and become an epidemic. The fact that biofilm formation seems to inevitably happen is due to factors such as the
389 large number of lineages that encounter the surface, and the existence of multigenerational memory, which can
390 mitigate against initial failure to attach by conditioning a planktonic population primed for improved subsequent
391 attachment.

392 Indeed, a recent study applied a variation of our approach to antibiotic treatment of bacteria (39). In fact, the
393 quantitative evolution of bacterial populations in early biofilm formation is analogous to a time-reversed version of
394 antibiotic treatment: the nonprocessive regime of reversible attachment behaves like bacterial population dynamics for
395 antibiotic treatment well above the minimum inhibitory concentration (MIC). In the present study, however, we are able
396 to perform an unprecedented level of longitudinal comparison between theory and experiment. Because we have
397 information on the fates for every cell in a large number of bacterial lineages that occur during early biofilm formation,
398 we can directly measure and analyze the time evolution of the system. This analysis provides a conceptual framework
399 for understanding the taxonomy of surface colonization strategies and reveals an unanticipated difference between
400 PAO1 and PA14 behavior.

401 One of the old questions about biofilm formation is whether it is the newly landed cells or the dividing cells on the
402 surface that contribute more to the biomass increase in the biofilm. Our results suggest that not only is the answer

403 species and strain dependent, the question is misleading because of the assumed either-or format of the answer.
404 Surface sensing can evolve progenitor cells which land on a surface and commit almost its entire division lineage to the
405 surface, thereby drastically increase biomass.

406 Complementary surface colonization strategies: immediate vs deferred gratification

407 The “divide-detach” stochastic model highlights two distinct but complementary strategies for surface colonization that
408 are illustrated by PAO1 and PA14. For PAO1, surface population increase takes the form of the few families that are
409 more successful in retaining surface progeny. PAO1 families generally stay on the surface during biofilm formation, likely
410 due to the Wsp surface sensing system and Psl EPS secretion. Previous work has shown that early surface attachment
411 behavior depends on EPS production via the Wsp system (9, 23). In contrast, for PA14, surface population increase takes
412 the form of many families that are less successful in retaining surface progeny due to surface detachment. However,
413 PA14 cells can “remember” the surface due to the Pil-Chp system and multigenerational cAMP-TFP memory (8), which
414 primes them for biofilm formation whether they are currently on the surface or not and eventually leads to progressive
415 suppression of motility appendage activity. Both strategies are viable for surface colonization. PAO1 cells tend to attach,
416 increase their surface population more quickly, and persist longer on a surface compared to PA14, which suggests that
417 PAO1 can potentially attach to surfaces even in ecologically crowded environments or successfully form biofilms by
418 outgrowing competing species. Indeed, this has been experimentally observed: EPS-producing *P. aeruginosa* strains tend
419 to persist on surfaces better than EPS nonproducers, despite possible exploitation by “cheaters” that can potentially use
420 the communal good of EPS (40). In contrast, PA14 exposed to a surface do not initially stay on the surface, and slowly
421 increase surface coverage. Rather, they form a surface-sentient planktonic population that can quickly attach and
422 colonize the surface later in time, which may be better adapted for overwhelming host defense (i.e., a naïve surface)
423 rather than microbial competition. Moreover, it is interesting to note that EPS secretion is extracellular and can be
424 shared spatially and temporally with both neighbors from different lineages and descendants in close proximity (41),
425 whereas memory is intracellular and can be only passed down temporally through division.

426 It is possible that our observations and results with PAO1 and PA14 may be generalizable to other *P. aeruginosa* strains.
427 The majority of strains in the International *Pseudomonas* Consortium Database (IPCD) can be identified as either PAO1-
428 like or PA14-like based on their phylogeny (i.e., same phylogenetic sub-group as either PAO1 or PA14) (42-45).
429 Consistent with our results, crystal violet biofilm assays show that the PAO1-like strains seem to produce early biofilms
430 faster than the PA14-like strains (Figure S6). Although it is clear from the data spread that there is more to
431 *Pseudomonad* phylogenetic diversity than biofilm behavior, this observation suggests that the phylogenetic distance
432 from either PAO1 or PA14 could be incorporated into a metric for categorizing a *P. aeruginosa* strain’s biofilm formation
433 behavior as either PAO1-like or PA14-like. It is tempting to draw an analogy between differences in these strategies to
434 differences in “immediate-” vs “deferred-gratification” behavior in a prototypical cognitive-affective processing system,
435 with the latter correlating to successful outcomes in complex competitions (46). For *P. aeruginosa*, there is no cognition
436 of course, but the existence of a specific sensing cascade for PA14 effectively encodes the analog of “deferred-
437 gratification” behavior at a molecular level. Indeed, PA14 is usually considered to be more virulent than PAO1 (47).
438 However, it is likely that these bacterial strategies have their own advantages under different circumstances.
439 Furthermore, our model can be applied to other bacterial systems to understand how they utilize their cellular
440 machinery for various surface colonization strategies.

441 Materials and Methods

442 Strains and growth conditions

443 *Pseudomonas aeruginosa* PAO1 and PA14 wild type (WT) strains were used in this study. For the flagellum localization
444 data, PA14 WT and $\Delta pilA$ (deleting the major subunit of the TFP filament) (48) with FliC (the major subunit of the
445 flagellum filament) modified to FliC(T394C) (49) were used. PAO1 was cultured as previously described (21, 23), and
446 PA14 was cultured as previously described (8). Culturing protocols are summarized as follows. Bacteria were plated on
447 LB agar plates and incubated at 37 °C overnight. Individual colonies were swabbed from the plate and grown overnight
448 for ~18 h in an incubator at 37 °C shaking at 220 rpm. Overnight cultures were regrown in the same overnight growth

449 conditions to an $OD_{600nm} \sim 0.4-0.6$. Regrowth cultures were then diluted in flow cell conditions to an $OD_{600nm} \sim 0.01-$
450 0.03 . These final diluted cultures were used for injection into the flow chamber.

451 Different medium conditions were chosen for PAO1 and PA14 based on the medium optimized for flow cell early biofilm
452 formation experiments for each individual strain in prior work. For PAO1, overnight and regrowth media consisted of
453 FAB medium with 30 mM glutamate, while flow cell media consisted of FAB medium with 0.6 mM glutamate (21, 23).
454 For PA14, overnight and regrowth media consisted of M63 medium with 1 mM magnesium sulfate, 0.2% glucose, and
455 0.5% casamino acids (CAA), while flow cell media consisted of M63 medium with 1 mM magnesium sulfate, 0.05%
456 glucose, and 0.125% CAA (8, 48). For flagellum staining experiments, the flow cell media also contained 0.375 $\mu\text{g}/\text{mL}$
457 Alexa Fluor 488 C5 maleimide dye (Molecular Probes). For more details on the culturing procedures, please refer to the
458 corresponding references. PAO1 experiments were repeated with the PA14 medium conditions, and the same basic
459 trends discussed in this paper still hold.

460 Crystal violet biofilm assays

461 Biofilm assays were performed as previously described with minor modifications (50, 51). Briefly, culture inocula were
462 grown in 100 μL of LB medium at 37 °C in a 96-well microtiter plate for ~ 16 h. Cultures were normalized and diluted
463 $\sim 1:100$ in M63 medium with 1 mM magnesium sulfate and 0.4% arginine (instead of glucose and CAA). To a 96-well
464 microtiter plate, 100 μL of the diluted culture was added to each well. Microtiter plates were then incubated at 37 °C for
465 24 h in a humidified environment to prevent culture evaporation. To remove unattached bacteria and spent medium,
466 the microtiter dishes were inverted, then washed twice by gently immersing the plate in tap water followed by removing
467 the liquid by briskly inverting the plate. Microtiter dish biofilms were stained by addition of 125 μL of 0.1% (w/v) crystal
468 violet to each well, and incubation for 15 min at room temperature. After the crystal violet solution was removed, the
469 plates were washed three times, as described above, with tap water. Plates were allowed to air-dry overnight. The
470 amount of crystal violet retained by each biofilm was measured by adding 150 μL of 30% (v/v) glacial acetic acid,
471 incubating for 15 min at room temperature, and mixing by pipetting. Transfer of 100 μL of this mixture to a 96-well clear
472 flat-bottom plate enabled spectrophotometric analysis at 550 nm. Each assay included 4 measurements (technical
473 replicates), which were averaged, and the experiment was performed 5 times (biological replicates). The strains used in
474 these assays are shown in Table S1. *P. aeruginosa* strains PAO1 and PA14 were initially described in (52) and (47),
475 respectively. All clinical and environmental *P. aeruginosa* isolates were from the International *Pseudomonas* Consortium
476 Database (IPCD) (43). These strains have both been phenotypically and genotypically characterized (44, 45).

477 Flow cell experiments and data acquisition

478 Flow cells were prepared and inoculated as previously described (8) with the following modifications. Flow cells were
479 purchased from two sources: Department of Systems Biology, Technical University of Denmark, and Ibidi (sticky-slide
480 *VI*^{0.4} with a glass coverslip). An in-line injection port (Ibidi) was used at the inlet for inoculating bacteria into the flow
481 cell. For Ibidi flow cells, elbow connectors (Ibidi) were used to connect the chamber with tubing. The diluted bacteria
482 culture was injected into the flow cell and allowed to incubate for 10-20 min without flow on the heating stage at 30 °C.
483 Flow was then started at 3 mL/h for the entire acquisition time.

484 Images were taken using either an Andor iXon EMCCD camera with Andor IQ software on an Olympus IX81 microscope
485 equipped with a Zero Drift Correction autofocus system or an Andor Neo sCMOS camera with Andor IQ software on an
486 Olympus IX83 microscope equipped with a Zero Drift Correction 2 continuous autofocus system. Bright-field images
487 were taken every 3 s (30 ms exposure time) on the IX81 system and every 100 ms (30 ms exposure time) on the IX83
488 system. For flagellum staining experiments, bright-field images were taken every 3 s (30 ms exposure time) on the IX81
489 system, and two fluorescence images (+0 and +1 μm above the imaging focal plane) were taken every 15 min (100 ms
490 exposure time) using a Lambda LS (Sutter Instrument) xenon arc lamp and a GFP filter. On the IX81 system, total
491 acquisition time was ~ 40 h, resulting in ~ 48000 images. On the IX83 system, total acquisition time was ~ 20 h, resulting in
492 720000 images. Image size was 67 $\mu\text{m} \times 67 \mu\text{m}$ (1024 \times 1024 pixels).

493 Multigenerational family tracking analysis

494 Image analysis, family tracking and manual validation, family tree plotting, and tree asymmetry calculations were
 495 performed in MATLAB as previously described (8) without modification. Fluorescence images were processed as follows
 496 to reduce noise and background signals and enhance flagella signals. Bandpass filtering, gamma correction, intensity
 497 percentile normalization, and then a green colormap were applied to the images. Fluorescence images were then
 498 overlaid on top of bright-field images using the lighten opacity setting. Probability distributions were obtained from the
 499 family trees as follows. The experimental probability distribution $P_n(t)$ is a 2D matrix, where the columns represent n ,
 500 the number of cells present in one family, and each row is a time step t , the experimental image data acquisition interval
 501 (either every 3 s or 100 ms, depending on the data). For each time step t (in terms of lineage time, with each family
 502 starting at $t_{\text{lineage}} = 0$), we keep track of how many families have $n = 0$ cells, $n = 1$ cell, $n = 2$ cells, and so on. The
 503 proportion of families with $n = 0, 1, 2, \dots$ cells then become one row in the matrix. This is equivalent to generating a
 504 histogram for $X_t(\omega)$ using the states Σ as the bins. The full matrix is generated by repeating this for all time steps in the
 505 experimental data. Experimental moments were calculated by the formula $\langle n(t)^k \rangle = \sum_{n=0}^{\infty} n^k P_n(t)$, where $P_n(t)$ is the
 506 experimental probability distribution. MATLAB functions from the base installation of MATLAB R2015a, Statistics and
 507 Machine Learning Toolbox, Curve Fitting Toolbox, Image Processing Toolbox, Signal Processing Toolbox, and custom
 508 MATLAB functions were used for all analyses. In particular, the MATLAB functions “fit”, “fmincon”, and “ode45” were
 509 used for function fitting, nonlinear least-squares minimization with constraints, and numerical integration.

510 Divide-detach stochastic model equations

511 Explanation of the model is given in the main text. The solution for the master equation (eq. 1), which is the model
 512 probability distribution $P_n(t)$, is given by

$$P_n(t) = \begin{cases} 1 - \frac{\exp(-\rho(t))}{W(t)}, & n = 0 \\ \frac{\exp(-\rho(t))}{W(t)^2} \left(1 - \frac{1}{W(t)}\right)^{n-1}, & n > 1 \end{cases}, \quad 2$$

$$W(t) = \exp(-\rho(t)) \left(1 + \int_0^t \mu(\tau) \exp(\rho(\tau)) d\tau\right),$$

$$\rho(t) = \int_0^t (\mu(\tau) - \lambda(\tau)) d\tau,$$

513 and $\lambda(t)$ and $\mu(t)$ are the single cell division and detachment rates, respectively. Both rates are functions of time and
 514 positive (i.e., $\lambda(t) > 0$ and $\mu(t) > 0$).

515 The first and second model moments are given by the following equations and the linear form of the rates, $\lambda(t) = L_0 +$
 516 $L_1 t$ and $\mu(t) = C_0 + C_1 t$, which are used for fitting the experimental moments

$$\langle n(t) \rangle = \exp \left[(L_0 - C_0)t - \frac{1}{2}(C_1 - L_1)t^2 \right], \quad 3$$

$$\langle n(t)^2 \rangle = \exp[2(L_0 - C_0)t - (C_1 - L_1)t^2] \left[1 + (L_0 + C_0) \int_0^t \exp \left[-(L_0 - C_0)\tau + \frac{1}{2}(C_1 - L_1)\tau^2 \right] d\tau \right. \\ \left. + (C_1 + L_1) \int_0^t \tau \exp \left[-(L_0 - C_0)\tau + \frac{1}{2}(C_1 - L_1)\tau^2 \right] d\tau \right]. \quad 4$$

517 Evaluating the integral analytically in eq. 4 depends on the relative signs of $\{L_0, L_1, C_0, C_1\}$.

518 Analytical solutions to the equations in the stochastic model

519 The solution for the master equation (eq. 1), which is the model probability distribution $P_n(t)$, can be found by using the
 520 so-called generating function

521

$$G(z, t) = \sum_{n=0}^{+\infty} z^n P_n(t).$$

522 By plugging in the generating function into eq. 1, we obtain

$$\partial_t G(z, t) = (1 - z)(\lambda z + \mu) \partial_z G(z, t). \quad 5$$

523 We can rewrite the previous equation in a Ricatti's form, which reads

$$\frac{dz}{dt} = S + Qz + Rz^2,$$

525 where $S = -\mu$, $Q = (\lambda + \mu)$, and $R = -\lambda$. A particular solution of the previous equation is given by Y . Then the
526 previous equation can be solved by quadrature $z(t) = x(t) + Y(t)$ and

$$\frac{dx}{dt} = [S + 2YQ]x + QY^2.$$

528 A change of variables $u = \frac{1}{x} = \frac{1}{z - Y}$ yields

$$\frac{du}{dt} = [S + 2YQ]u + Q.$$

530 The solution of the Ricatti's equation (53) is a homographic function

$$u = C \exp\left(\int [S + 2YQ] dt\right) + U,$$

532 where C is an arbitrary constant and U is a particular solution. We can rewrite u as

$$u = C\psi + \phi,$$

534 and the solution for z reads

$$z = Y + \frac{1}{C\psi + \phi} = \frac{C\psi Y + \phi Y}{C\psi + \phi} = \frac{C\alpha + \beta}{C\gamma + \delta}.$$

536 By using the Palm's formulae (31-33, 35, 54), it is possible to find $P_0(t)$ and $P_n(t)$ as a function of η_t and ξ_t , two
537 unknown functions, which reads

$$P_0(t) = \xi_t, \text{ and } P_n(t) = (1 - P_0(t))(1 - \eta_t)\eta_t^{n-1}.$$

539 By means of geometric series, the generating function $G(z, t)$ reads

$$G(z, t) = \frac{\xi_t + (1 - \xi_t - \eta_t)z}{1 - \eta_t z}.$$

541 By plugging back this equation into eq. 5, we can find ξ_t and η_t and finally the solution (eq. 2).

542 To compare the model with the experimental results, we use the model moments defined as

$$\langle n(t)^k \rangle = \sum_{n=0}^{\infty} n^k P_n(t).$$

544 From the master equation (eq. 1), we can find

$$\frac{d}{dt} \langle n(t)^k \rangle = \sum_{n=0}^{\infty} n^k \frac{d}{dt} P_n(t) = \sum_{n=0}^{\infty} [((n+1)^k - n^k)\lambda(t) - (n^k - (n-1)^k)\mu(t)] n P_n(t).$$

545

546 The first moment reads

$$\begin{aligned}
 547 \quad \frac{d}{dt} \langle n(t) \rangle &= \sum_n n \frac{d}{dt} P_n(t) \\
 548 \quad &= -(\lambda + \mu) \sum_n n^2 P_n(t) + \mu \sum_n (n^2 + n) P_{n+1}(t) + \lambda \sum_n (n^2 - n) P_{n-1}(t) \\
 549 \quad &= \lambda \sum_{n=1} [(n-1)^2 P_{n-1}(t) + (n-1) P_{n-1}(t)] + \mu \sum_{n=0} [(n+1)^2 P_{n+1}(t) - (n+1) P_{n+1}(t)] - (\lambda + \mu) \sum_{n=0} n^2 P_n(t) \\
 550 \quad \Leftrightarrow \frac{d}{dt} \langle n(t) \rangle &= \lambda [\langle n(t)^2 \rangle + \langle n(t) \rangle] + \mu [\langle n(t)^2 \rangle - \langle n(t) \rangle] - (\lambda + \mu) \langle n(t)^2 \rangle \\
 551 \quad \Rightarrow \frac{d}{dt} \langle n(t) \rangle &= (\lambda - \mu) \langle n(t) \rangle.
 \end{aligned}$$

552 The solution to this differential equation is

$$553 \quad \langle n(t) \rangle = n(0) \exp(-\rho), \quad n(0) = 1, \quad \rho(t) = \int_0^t (\mu(\tau) - \lambda(\tau)) d\tau.$$

554 Plugging in the linear form of the rates, $\lambda(t) = L_0 + L_1 t$ and $\mu(t) = C_0 + C_1 t$, yields eq. 3.

555 The second moment (again, using the linear form of the rates, $\lambda(t) = L_0 + L_1 t$ and $\mu(t) = C_0 + C_1 t$) reads

$$\begin{aligned}
 556 \quad \frac{d}{dt} \langle n(t)^2 \rangle &= \sum_{n=0}^{\infty} [((n+1)^2 - n^2)(L_0 + L_1 t) - (n^2 - (n-1)^2)(C_0 + C_1 t)] n P_n(t) \\
 557 \quad &= \langle n(t) \rangle (L_0 + L_1 t + C_0 + C_1 t) + 2 \langle n(t)^2 \rangle (L_0 + L_1 t - C_0 - C_1 t).
 \end{aligned}$$

558 Elementary computations yield eq. 4.

559 [Hydrodynamic model of TFP retraction during flagellum-mediated spinning](#)

560 We adapt the hydrodynamic model that we developed previously (37) to investigate the effects of TFP on flagellum-mediated spinning. Here, we consider a bacterium consisting of a cylindrical body attached to the surface at the pole opposite the flagellum, a helical filament for the flagellum of equal length to the body, and a straight filament 2/3 of the body length for a pilus protruding from the body. We use resistive force theory (55) to relate the angular velocities of each component of the bacterium to the torques from the flagellar motor, the viscous resistance from the fluid, and the flagellar hook which resists bending between the head and the flagellum. The resultant model is used to consider how TFP affect the angle that the bacterium makes with the surface during flagellum-mediated spinning and thereby “stand up” to a near vertical orientation commonly observed before detachment.

568 We use the example where the ratio of hook stiffness to motor torque is 0.5 to show the effects of TFP (see (37) for details of the stiffness/motor torque ratio). We show time using units of seconds and a torque value of 2 pN μ m. We observe two significant effects on the surface angle when TFP retract during spinning: (i) the bacterium decreases its surface angle after retraction, (ii) the amplitude of oscillations in surface angle decreases after retraction. The opposite occurs when TFP extend during spinning: (i) the bacterium increases its surface angle after extension, (ii) the amplitude of oscillations in surface angle increases after extension. The strength of these effects depends on the choice of value of the flagellar motor torque and hook stiffness in the hydrodynamic model.

575 [TFP and flagellum activity metrics](#)

576 To characterize appendage activity during family tree tracking, we use the algorithms previously described (8) for TFP activity and adapt them for flagellum activity. As previously described, TFP activity is inferred by recognizing surface translational motion, which is the predominant behavior for TFP-driven motion for *P. aeruginosa* cells that attach to the

579 surface during early biofilm development. Analogous to this, the most common mode of flagellum activity is surface-
580 attached “spinning,” where cells attach via one pole on the surface, and spin at angular velocities consistent with typical
581 flagellum motor output (~ 5 rad/s) (36, 37). So, flagellum activity is inferred by recognizing surface rotational motion.
582 Based on the majority of flagellum-mediated surface spinning behavior producing trajectories that are tightly clustered
583 together and have strongly subdiffusive MSDs, the multi-parameter metric for flagellum activity is defined as follows. A
584 bacterium has flagellum activity during a given time point when it is “spinning” and has non-zero displacement over a w
585 frame moving window every $w/10$ frames. A cell that is “spinning” is defined as having the following characteristics
586 during the w frame window: a Mean Squared Displacement (MSD) slope of less than 0.9 and having the maximum 2
587 point distance of its trajectory being greater than or equal to 15% of its maximum cell body length and less than its cell
588 body length. As previously described, a value of $w = 100$ was used (8).

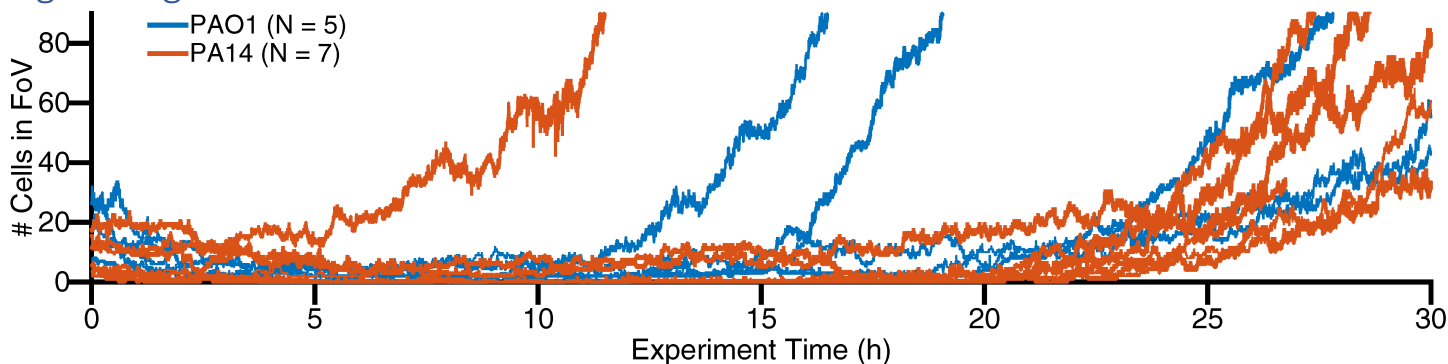
589 Acknowledgements

590 CKL, GCLW, and MRP are supported by the Army Research Office (W911NF-18-1-0254). CKL, GCLW, and GAO are
591 supported by the National Institutes of Health (1R01AI143730-01). KZ is supported by the National Key R&D Program of
592 China (2018YFA0902102). RLT is supported by the Amgen Scholars U.S. Program.

593 We thank Joshua A. Keefe and Joshua S. Helali for their contributions to the initial family tree data validation during the
594 early stages of this work.

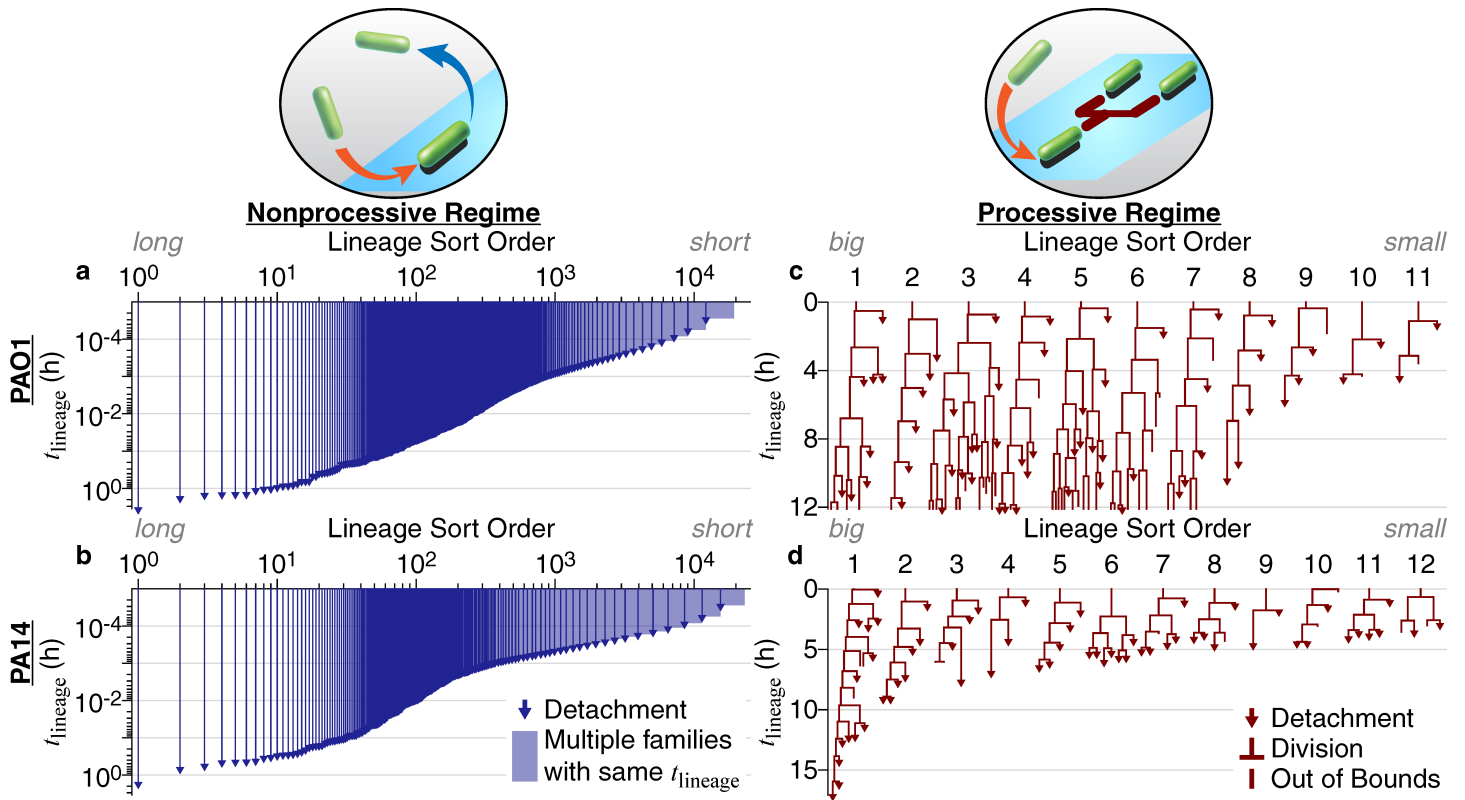
595 Competing interests: none

596 Figure Legends

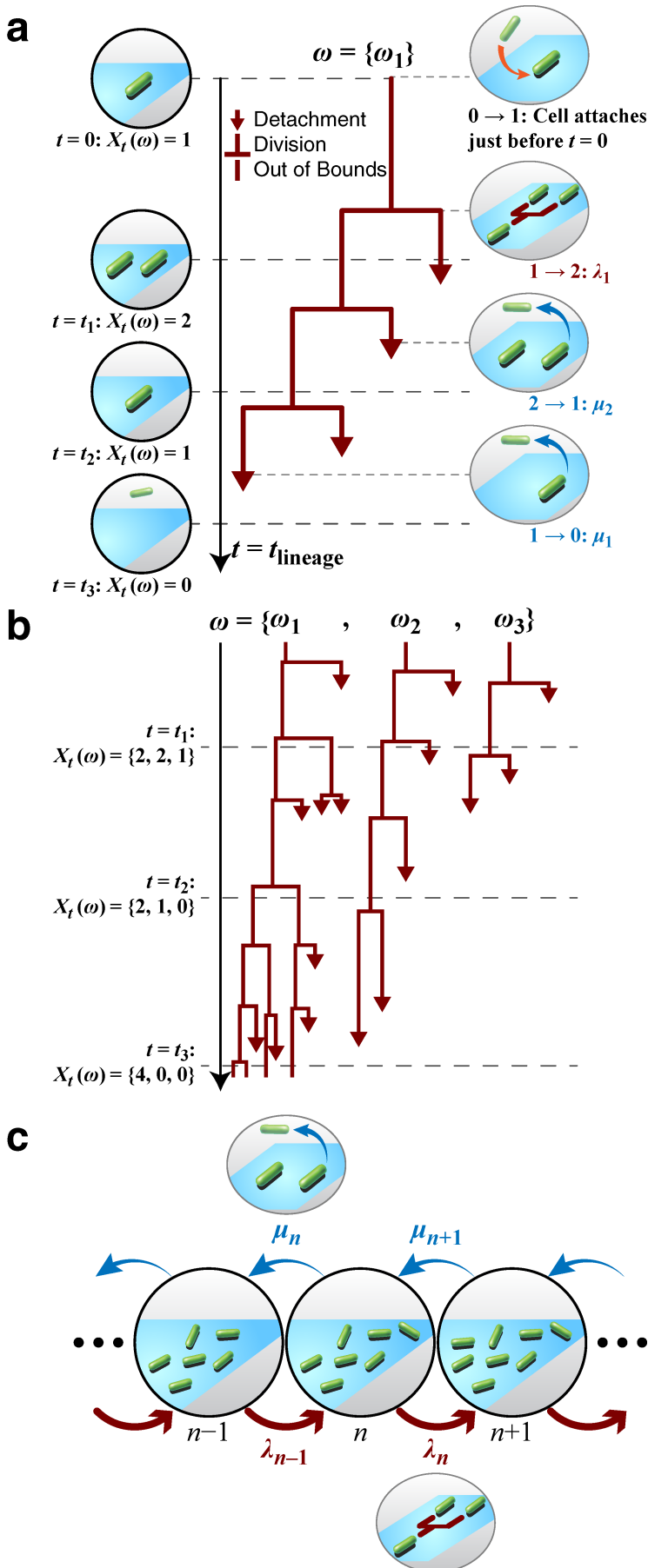


597

598 Figure 1. PAO1 and PA14 can both form biofilms and have similar trends of exponential surface population increase.
599 Each line represents one experiment where we count how many cells are in a single field of view (FoV) for WT PAO1 and
600 PA14 as experiment time progresses (5 and 7 independent experiments for PAO1 and PA14, respectively). Experiment
601 time = 0 h corresponds to when imaging commenced after cells were inoculated into the flow cell chamber. Both PAO1
602 and PA14 have the variable lag period and the exponential increase, which is consistent with the fact that both strains
603 initially undergo reversible attachment, and then subsequently form biofilms.



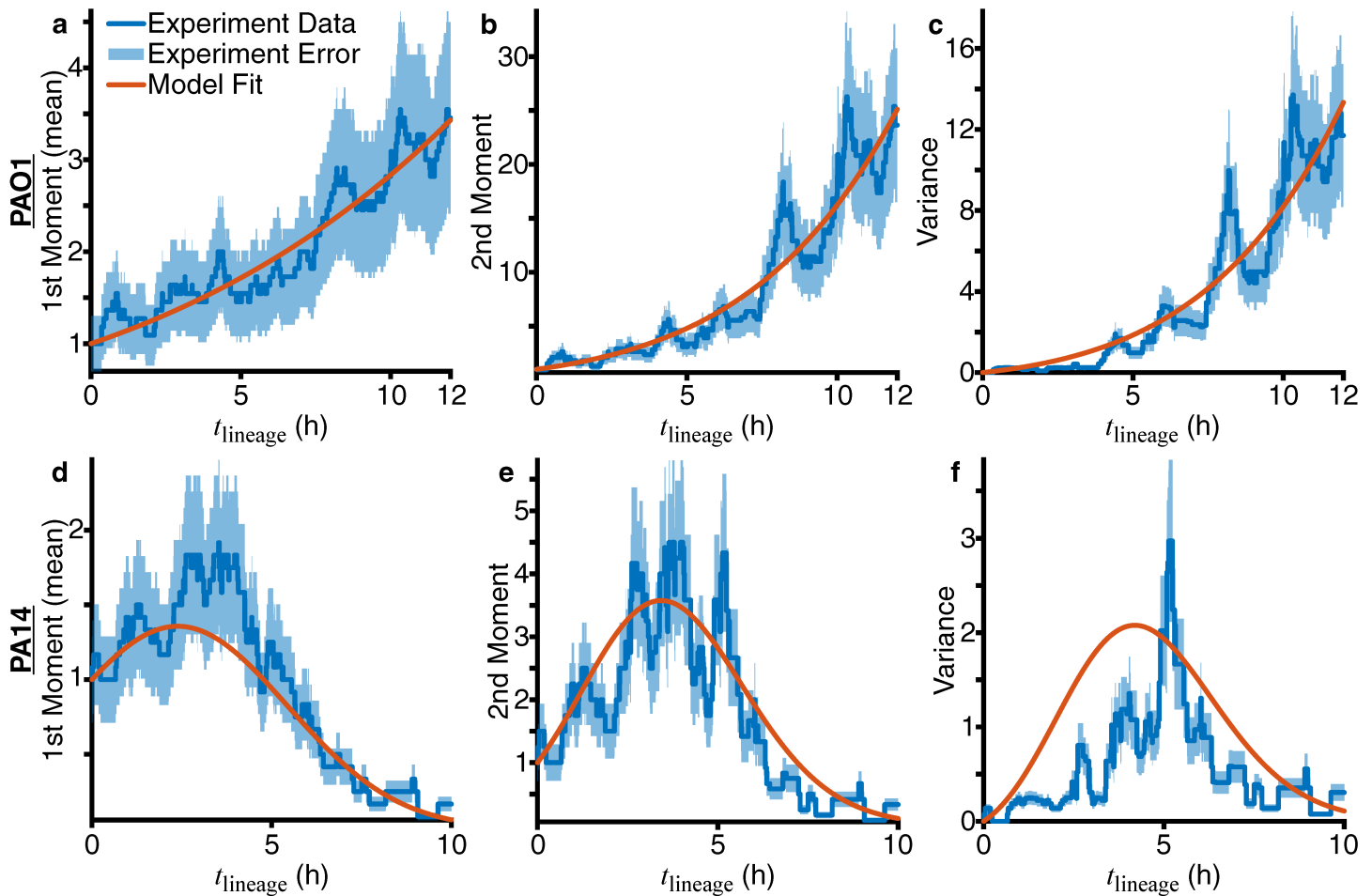
604
 605 Figure 2. PAO1 and PA14 family trees in different regimes of reversible attachment. (a,b) Families in the nonprocessive
 606 regime of reversible attachment, which is when cells detach before dividing. Both axes are on a log scale. In this
 607 nonprocessive regime, PAO1 has $m = 19353$ tracked families, and PA14 has $m = 23104$ tracked families. Note the
 608 similarities between PAO1 and PA14. (c,d) Families in the processive regime of reversible attachment, which is when
 609 cells divide at least once before detaching. Both axes are on a linear scale. Each family start at $t_{\text{lineage}} = 0$ h when the
 610 founder cell attaches to the surface. Tracking continues for that family until either all members detach, or we lose track
 611 of the family (where we can no longer distinguish individual cells, or the cells move out of the recording boundaries). We
 612 then record this time as the family's residence time. For each regime and strain, we sort families by residence times in
 613 descending order, which sorts them by the amount of time that they have continuously contacted the surface. In this
 614 processive regime, families here are used for the model and are a subset of the full tracked families shown in Figure S3.



615

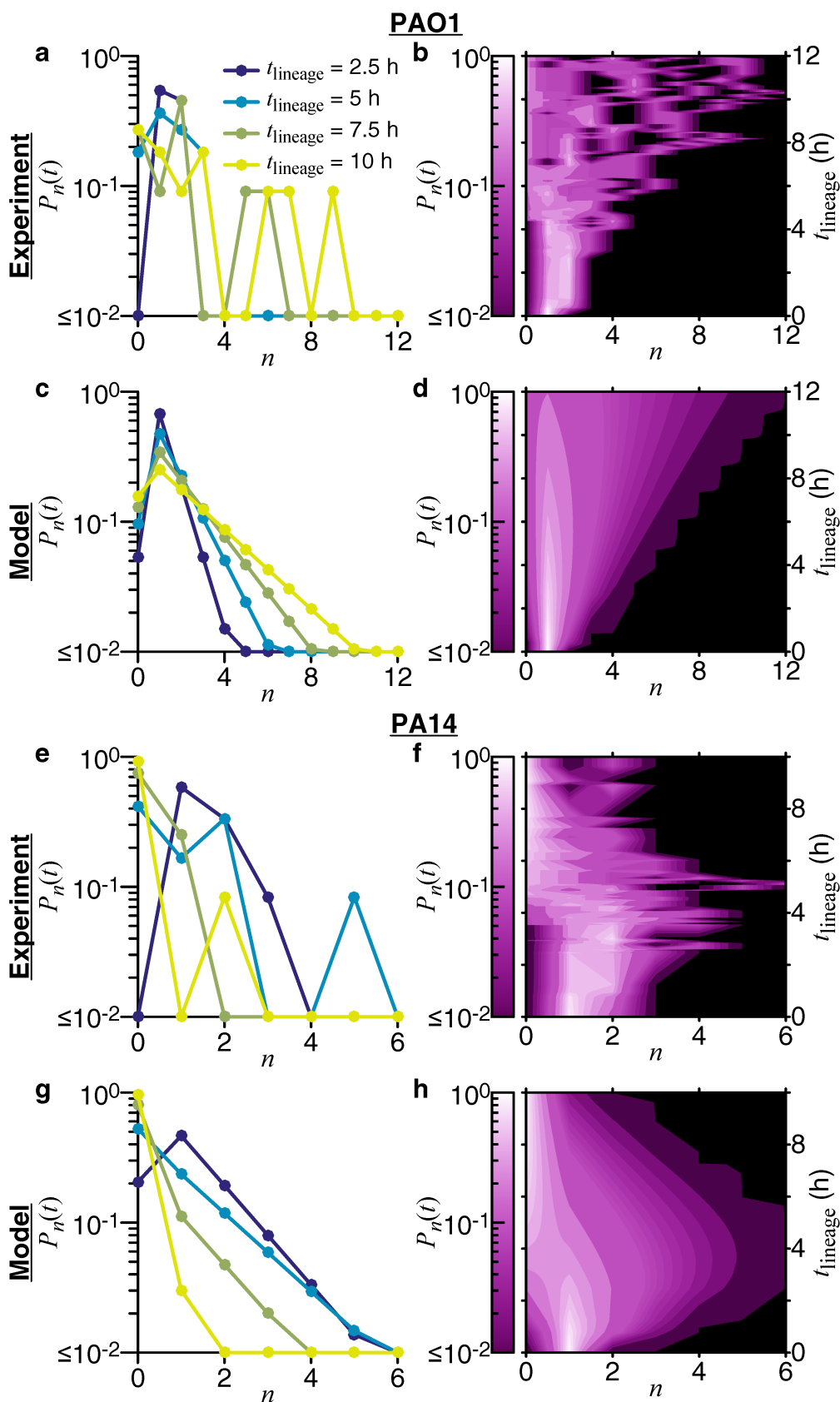
616 Figure 3. Family trees are a stochastic process. (a) Example illustrating the stochastic process with $m = 1$ family tree. In
 617 this case, at time t , $X_t(\omega)$ is the number of observed cells in the family tree $\omega = \{\omega_1\}$ at time t . Attachment of the

founder cell happens just before time $t = t_{\text{lineage}} = 0$, so it is not explicitly captured by this process. When a cell divides, it undergoes a transition $n \rightarrow n + 1 = \lambda_n$, and when it detaches, it undergoes a transition $n \rightarrow n - 1 = \mu_n$, where n is the state (i.e., number of observed cells) before the transition. (b) Example illustrating the stochastic process with $m = 3$ family trees. At time t , $X_t(\omega) = \{X_t^1(\omega_1), X_t^2(\omega_2), X_t^3(\omega_3)\}$ are the number of observed cells for each of the family trees $\omega = \{\omega_1, \omega_2, \omega_3\}$. (c) Dynamics of the stochastic process for state n . As shown in part (a), a transition $n \rightarrow n + 1 = \lambda_n$ occurs when a cell divides, and a transition $n \rightarrow n - 1 = \mu_n$ occurs when a cell detaches.



624

625 Figure 4. Obtaining division (λ) and detachment (μ) rates by fitting experimental and model moments of the number of
 626 cells in a family for families in the processive regime of reversible attachment. Moments and variance calculated from
 627 experimental data are plotted as blue lines, with the relative error (calculated as $1/\sqrt{m}$, where m is the number of
 628 families used) shown as the light blue shaded area. Variance is defined as the second moment minus the first moment
 629 squared. Red lines show the fits to the first and second moments (eq. 3-4) using nonlinear least-squares. For the model,
 630 we use the linear functional form of the rates, $\lambda(t) = L_0 + L_1 t$ and $\mu(t) = C_0 + C_1 t$. The resulting coefficients from the
 631 fits are as follows: for PAO1, $L_0 = 0.136 \text{ h}^{-1}$, $L_1 = 0 \text{ h}^{-2}$, $C_0 = 0.0242 \text{ h}^{-1}$, $C_1 = 0.00147 \text{ h}^{-2}$, and for PA14, $L_0 =$
 632 0.256 h^{-1} , $L_1 = 0 \text{ h}^{-2}$, $C_0 = 0 \text{ h}^{-1}$, $C_1 = 0.107 \text{ h}^{-2}$.



633

634

635

636

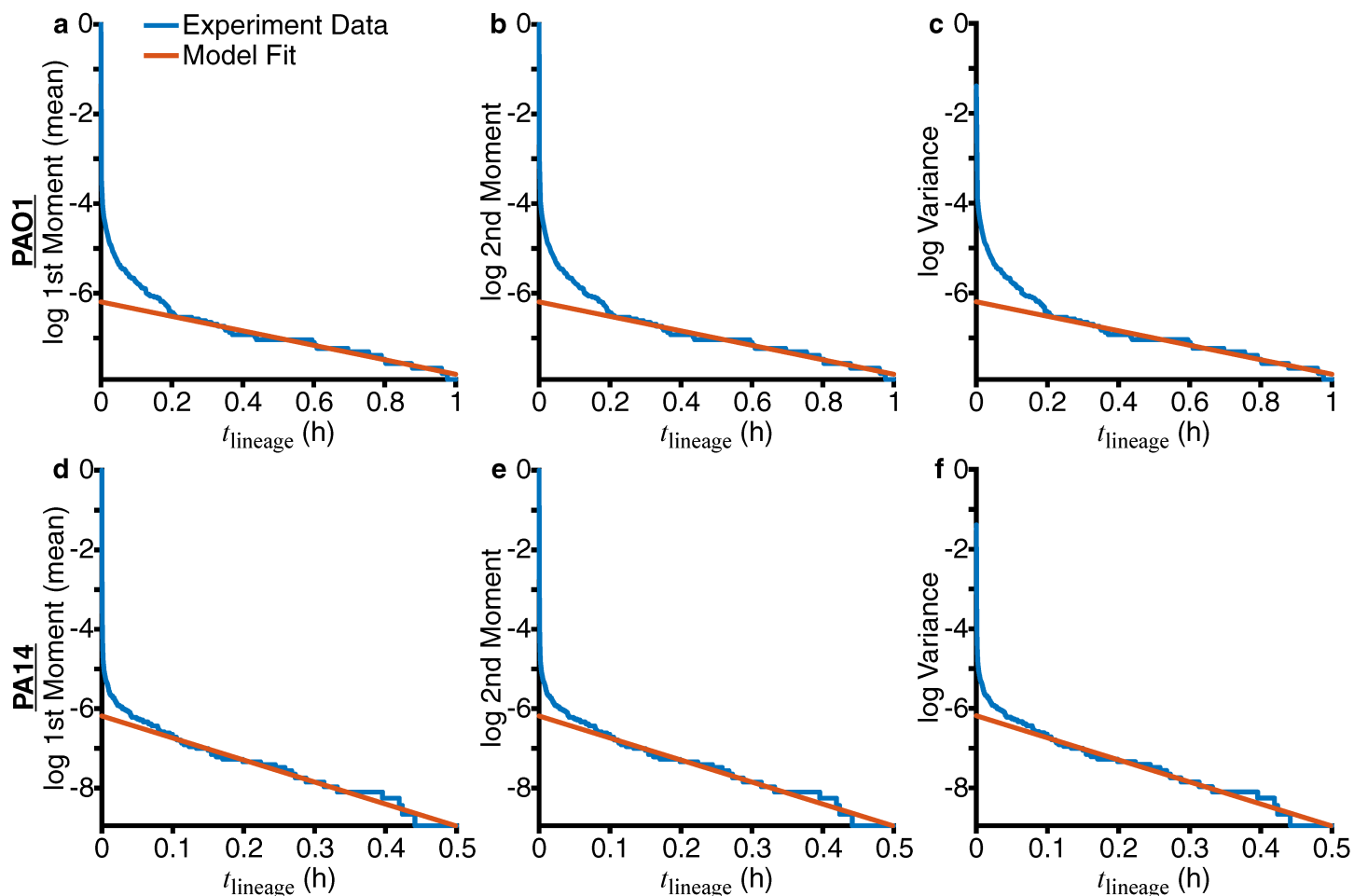
637

638

639

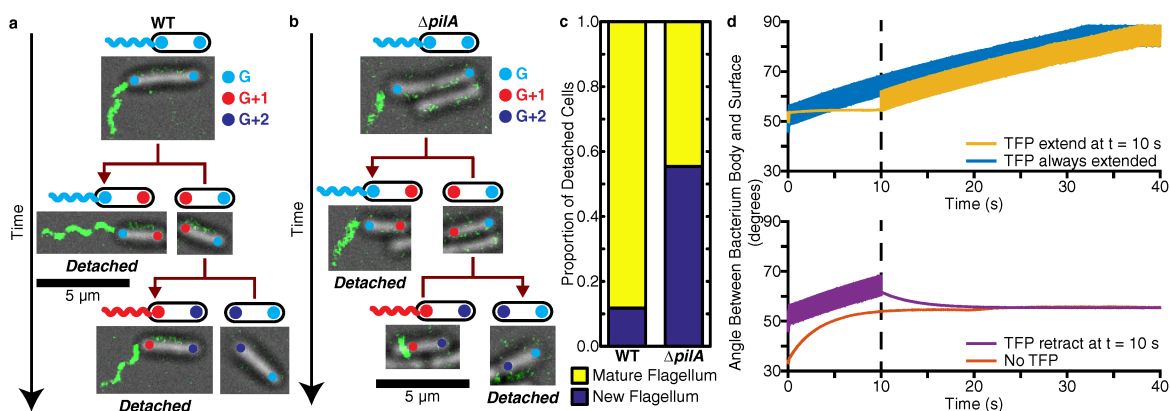
Figure 5. Comparing experimental and model probability distributions for the number of cells in a family for families in the processive regime of reversible attachment. Experimental probability distributions are built directly from the data, as described in the methods (section “Multigenerational family tracking analysis”). For the model probability distribution $P_n(t)$, we use eq. 2 and the linear functional form of the rates, $\lambda(t) = L_0 + L_1 t$ and $\mu(t) = C_0 + C_1 t$. The model rate coefficients used are shown in Figure 4. Probability distributions are compared in two different ways. The left column shows plots of $P_n(t)$ vs n for specific lineage times $t = \{2.5, 5, 7.5, 10\}$ h, and the right column shows plots of the entire

640 $P_n(t)$ vs n and t , where the probability is represented by the shades of color in the contour plots. Probabilities are
 641 shown on a log scale.



642

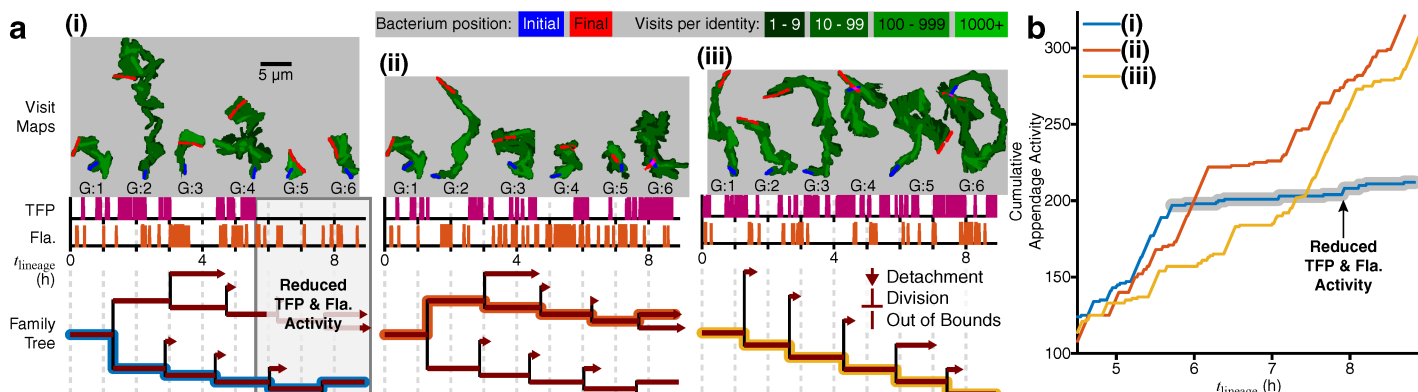
643 Figure 6. Fitting experimental moments show that families in the nonprocessive regime of reversible attachment have
 644 only detachment events. The natural logarithm (log) of the moments and variance calculated from experimental data
 645 are plotted as blue lines. Relative errors (calculated as $1/\sqrt{m}$, where m is the number of families used) are not plotted
 646 here, as $m \sim 20000$ for both PAO1 and PA14, and the values are very small. Red lines show the fits of the experimental
 647 data to the function $\log(y(t)) = a_1 t + a_0$. For PAO1, fits were performed for $0.2 \text{ h} \leq t \leq 1 \text{ h}$, with the resulting fit
 648 coefficients as $a_1 = -1.61 \text{ h}^{-1}$, $a_0 = -6.19$. For PA14, fits were performed for $0.1 \text{ h} \leq t \leq 0.5 \text{ h}$, with the resulting fit
 649 coefficients as $a_1 = -5.55 \text{ h}^{-1}$, $a_0 = -6.19$.



650

651 Figure 7. TFP and flagella are both important for the detachment process in PA14. (a,b) The location of the flagellum and
 652 the age of poles (measured in generations) can be tracked across multiple generations. The fluorescence image of the
 653 labeled flagellum is overlaid on top of the bright field image, and the poles are overlaid as colored circles (color

654 representing the pole generation G). Scale bars for the pictures are $5 \mu\text{m}$. (a) Example tracking for WT, where cells with
 655 mature flagella detach. (b) Example tracking for the $\Delta pilA$ mutant (deletion of the major subunit for the TFP filament),
 656 where one cell with a mature flagellum and one cell without a flagellum detach. (c) Proportion of detached cells with a
 657 mature flagellum vs a new flagellum (which includes no flagellum), calculated from 154 events for WT and 74 events for
 658 $\Delta pilA$. The proportions are statistically significantly different between the strains according to the χ^2 test ($p\text{-value} \ll$
 659 10^{-4}). (d) Angle that the bacterium's body makes with the surface for different TFP conditions in the hydrodynamic
 660 model: TFP extension at $t = 10 \text{ s}$ (top plot, yellow-orange), TFP retraction at $t = 10 \text{ s}$ (bottom plot, purple), TFP extended
 661 throughout (top plot, blue), and no TFP (bottom plot, red). If the bacterium does not spin, then the angle between the
 662 body and surface will stay at the (arbitrary) initial condition we have chosen in the model. We show time using units of
 663 seconds and a torque value of $2 \text{ pN } \mu\text{m}$ (37).



664

665 Figure 8. Family tree architecture controlled by generation-dependent motility activity. (a) TFP and flagellum activities
 666 are plotted for single branches of a family as magenta and red spike plots, with each spike representing one instance of
 667 activity. The colored line on the family tree plot traces the analyzed branch. We plot the corresponding visit map of each
 668 single cell (top, gray boxes), shown as shades of green in a logarithmic color scale with initial (final) positions shown in
 669 blue (red), to show the trajectory history and visual representation of TFP and flagellum activity. The size of each visit
 670 map is roughly proportional to the level of activity: cells with high TFP activity have elongated visit maps, while cells with
 671 high flagellum activity have circular visit maps. For WT, we see one example where TFP and flagellum activity are
 672 reduced and do not coincide, resulting in a division event where no daughter cells detach (i). The other examples show
 673 either higher activities or activities that coincide, resulting in a continuation of division events with detachment
 674 occurring (ii, iii). (b) Plot of the cumulative appendage activity (i.e., the cumulative number of instances of either TFP or
 675 flagellum activity) for the 3 examples in (a). For example (i), the curve plateaus out at $t_{\text{lineage}} \sim 6 \text{ h}$, which is when the
 676 reduction in appendage activity occurs. For examples (ii) and (iii), the curves continue to rise, which shows that the
 677 appendages are continuing to be active.

678

References

- 679 1. Singh PK, Schaefer AL, Parsek MR, Moninger TO, Welsh MJ, Greenberg EP. 2000. Quorum-sensing signals
 680 indicate that cystic fibrosis lungs are infected with bacterial biofilms. *Nature* 407:762-764.
- 681 2. Hall-Stoodley L, Costerton JW, Stoodley P. 2004. Bacterial biofilms: from the Natural environment to infectious
 682 diseases. *Nature Reviews Microbiology* 2:95.
- 683 3. Biteen JS, Blainey PC, Cardon ZG, Chun M, Church GM, Dorrestein PC, Fraser SE, Gilbert JA, Jansson JK, Knight R,
 684 Miller JF, Ozcan A, Prather KA, Quake SR, Ruby EG, Silver PA, Taha S, van den Engh G, Weiss PS, Wong GCL,
 685 Wright AT, Young TD. 2016. Tools for the Microbiome: Nano and Beyond. *ACS Nano* 10:6-37.
- 686 4. O'Toole GA, Wong GCL. 2016. Sensational Biofilms: Surface Sensing in Bacteria. *Curr Opin Microbiol* 30:139-146.
- 687 5. Hug I, Deshpande S, Sprecher KS, Pfohl T, Jenal U. 2017. Second messenger-mediated tactile response by a
 688 bacterial rotary motor. *Science* 358:531-534.
- 689 6. McCarter L, Hilmen M, Silverman M. 1988. Flagellar Dynamometer Controls Swarmer Cell Differentiation of *V.*
 690 *parahaemolyticus*. *Cell* 54:345-351.
- 691 7. Ellison CK, Dalia TN, Vidal Ceballos A, Wang JC-Y, Biais N, Brun YV, Dalia AB. 2018. Retraction of DNA-bound type
 692 IV competence pili initiates DNA uptake during natural transformation in *Vibrio cholerae*. *Nature Microbiology*
 693 3:773-780.

- 694 8. Lee CK, de Anda J, Baker AE, Bennett RR, Luo Y, Lee EY, Keefe JA, Helali JS, Ma J, Zhao K, Golestanian R, O'Toole
695 GA, Wong GCL. 2018. Multigenerational memory and adaptive adhesion in early bacterial biofilm communities.
696 Proceedings of the National Academy of Sciences 115:4471-4476.
- 697 9. Guvener ZT, Harwood CS. 2007. Subcellular Location Characteristics of the *Pseudomonas aeruginosa* GGDEF
698 Protein, WspR, Indicate that It Produces Cyclic-di-GMP in Response to Growth on Surfaces. Mol Microbiol
699 66:1459-1473.
- 700 10. O'Connor JR, Kuwada NJ, Huangyutitham V, Wiggins PA, Harwood CS. 2012. Surface Sensing and Lateral
701 Subcellular Localization of WspA, the Receptor in a Chemosensory-like System Leading to C-di-GMP Production.
702 Mol Microbiol 86:720-729.
- 703 11. Chen Y, Chai Y, Guo JH, Losick R. 2012. Evidence for cyclic Di-GMP-mediated signaling in *Bacillus subtilis*. Journal
704 of bacteriology 194:5080-5090.
- 705 12. Ferreira RB, Chodur DM, Antunes LC, Trimble MJ, McCarter LL. 2012. Output Targets and Transcriptional
706 Regulation by a Cyclic Dimeric GMP-Responsive Circuit in the *Vibrio parahaemolyticus* Scr Network. J Bacteriol
707 194:914-924.
- 708 13. Gomelsky M, Galperin MY. 2013. Bacterial second messengers, cGMP and c-di-GMP, in a quest for regulatory
709 dominance. The EMBO journal 32:2421-2423.
- 710 14. Romling U, Galperin MY, Gomelsky M. 2013. Cyclic di-GMP: the first 25 years of a universal bacterial second
711 messenger. Microbiology and molecular biology reviews : MMBR 77:1-52.
- 712 15. Jones CJ, Utada A, Davis KR, Thongsomboon W, Zamorano Sanchez D, Banakar V, Cegelski L, Wong GCL, Yildiz FH.
713 2015. C-di-GMP Regulates Motile to Sessile Transition by Modulating MshA Pili Biogenesis and Near-Surface
714 Motility Behavior in *Vibrio cholerae*. PLOS Pathogens 11:e1005068.
- 715 16. Zamorano-Sánchez D, Xian W, Lee CK, Salinas M, Thongsomboon W, Cegelski L, Wong GCL, Yildiz FH. 2019.
716 Functional Specialization in *Vibrio cholerae* Diguanylate Cyclases: Distinct Modes of Motility Suppression and c-
717 di-GMP Production. mBio 10:e00670-19.
- 718 17. Luo Y, Zhao K, Baker AE, Kuchma SL, Coggan KA, Wolfgang MC, Wong GCL, O'Toole GA. 2015. A Hierarchical
719 Cascade of Second Messengers Regulates *Pseudomonas aeruginosa* Surface Behaviors. mBio 6:1-11.
- 720 18. Persat A, Inclan YF, Engel JN, Stone HA, Gitai Z. 2015. Type IV Pili Mechanochemically Regulate Virulence Factors
721 in *Pseudomonas aeruginosa*. Proc Natl Acad Sci U S A 112:7563-7568.
- 722 19. Costerton JW, Stewart PS, Greenberg EP. 1999. Bacterial biofilms: a common cause of persistent infections.
723 Science 284:1318-22.
- 724 20. Huangyutitham V, Guvener ZT, Harwood CS. 2013. Subcellular Clustering of the Phosphorylated WspR Response
725 Regulator Protein Stimulates Its Diguanylate Cyclase Activity. mBio 4:e00242-13.
- 726 21. Armbruster CR, Lee CK, Parker-Gilham J, de Anda J, Xia A, Zhao K, Tseng BS, Hoffman LR, Jin F, Harwood CS,
727 Wong GCL, Parsek MR. 2019. Heterogeneity in surface sensing suggests a division of labor in *Pseudomonas*
728 *aeruginosa* populations. eLife 8:e45084.
- 729 22. Irie Y, Borlee BR, O'Connor JR, Hill PJ, Harwood CS, Wozniak DJ, Parsek MR. 2012. Self-produced
730 exopolysaccharide is a signal that stimulates biofilm formation in *Pseudomonas aeruginosa*. Proc Natl Acad Sci U
731 S A 109:20632-20636.
- 732 23. Zhao K, Tseng BS, Beckerman B, Jin F, Gibiansky ML, Harrison JJ, Luijten E, Parsek MR, Wong GCL. 2013. Psl Trails
733 Guide Exploration and Microcolony Formation in *Pseudomonas aeruginosa* Biofilms. Nature (London, U K)
734 497:388-391.
- 735 24. Colvin KM, Gordon VD, Murakami K, Borlee BR, Wozniak DJ, Wong GC, Parsek MR. 2011. The pel polysaccharide
736 can serve a structural and protective role in the biofilm matrix of *Pseudomonas aeruginosa*. PLoS Pathog
737 7:e1001264.
- 738 25. Sauer K, Camper AK, Ehrlich GD, Costerton JW, Davies DG. 2002. *Pseudomonas aeruginosa* Displays Multiple
739 Phenotypes during Development as a Biofilm. Journal of Bacteriology 184:1140-1154.
- 740 26. Davey ME, Caiazza NC, O'Toole GA. 2003. Rhamnolipid Surfactant Production Affects Biofilm Architecture in
741 *Pseudomonas aeruginosa* PAO1. Journal of Bacteriology 185:1027-1036.
- 742 27. Henrici AT. 1933. Studies of Freshwater Bacteria: I. A Direct Microscopic Technique. J Bacteriol 25:277-87.
- 743 28. Zobell CE, Allen EC. 1935. The Significance of Marine Bacteria in the Fouling of Submerged Surfaces. Journal of
744 Bacteriology 29:239-251.
- 745 29. Sanchez A, Golding I. 2013. Genetic Determinants and Cellular Constraints in Noisy Gene Expression. Science
746 342:1188-1193.

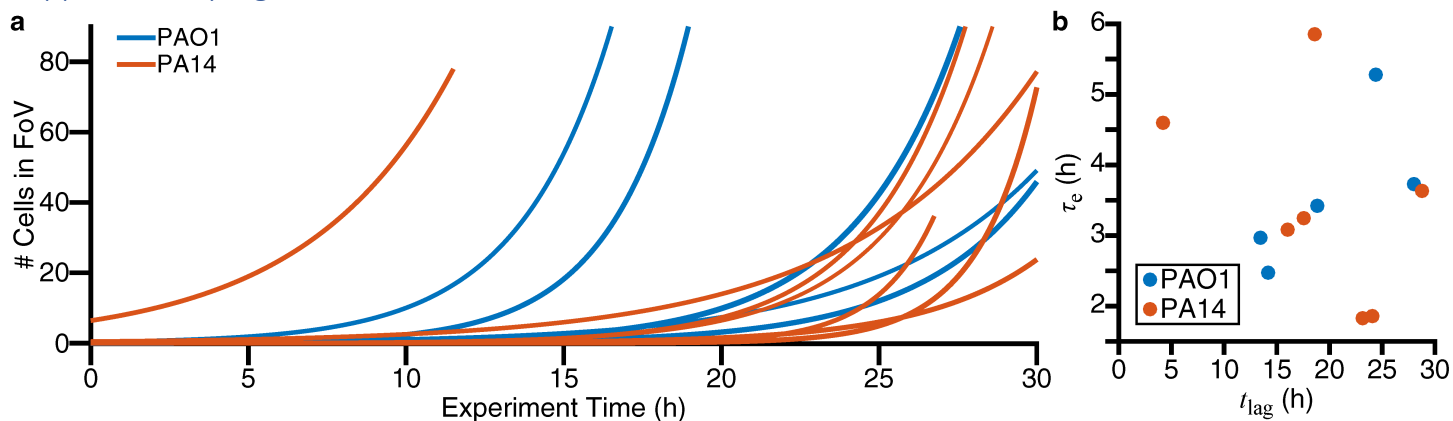
- 747 30. Shiryayev AN. 2012. Selected Works of AN Kolmogorov: Volume II Probability Theory and Mathematical
748 Statistics, vol 26. Springer Science & Business Media.
- 749 31. Arley N. 1949. On the "birth-and-death" process. Scandinavian Actuarial Journal 1949:21-26.
- 750 32. Kendall DG. 1949. Stochastic Processes and Population Growth. Journal of the Royal Statistical Society Series B
751 (Methodological) 11:230-282.
- 752 33. Kendall DG. 1948. On the Generalized "Birth-and-Death" Process. Ann Math Statist 19:1-15.
- 753 34. Novozhilov AS, Karev GP, Koonin EV. 2006. Biological applications of the theory of birth-and-death processes.
754 Briefings in Bioinformatics 7:70-85.
- 755 35. Feller W. On the Theory of Stochastic Processes, with Particular Reference to Applications, p 403-432. In (ed),
756 University of California Press,
- 757 36. Conrad JC, Gibiansky ML, Jin F, Gordon VD, Motto Da, Mathewson Ma, Stopka WG, Zelasko DC, Shrout JD, Wong
758 GCL. 2011. Flagella and Pili-Mediated Near-Surface Single-Cell Motility Mechanisms in *P. aeruginosa*. Biophys J
759 100:1608-1616.
- 760 37. Bennett RR, Lee CK, De Anda J, Neelson KH, Yildiz FH, O'Toole GA, Wong GCL, Golestanian R. 2016. Species-
761 Dependent Hydrodynamics of Flagellum-Tethered Bacteria in Early Biofilm Development. J R Soc, Interface
762 13:20150966.
- 763 38. Gibiansky ML, Conrad JC, Jin F, Gordon VD, Motto DA, Mathewson MA, Stopka WG, Zelasko DC, Shrout JD, Wong
764 GCL. 2010. Bacteria Use Type IV Pili to Walk Upright and Detach from Surfaces. Science (Washington, DC, U S)
765 330:197.
- 766 39. Coates J, Park BR, Le D, Şimşek E, Chaudhry W, Kim M. 2018. Antibiotic-induced population fluctuations and
767 stochastic clearance of bacteria. eLife 7:e32976.
- 768 40. Irie Y, Roberts AEL, Kragh KN, Gordon VD, Hutchison J, Allen RJ, Melaugh G, Bjarnsholt T, West SA, Diggle SP.
769 2017. The *Pseudomonas aeruginosa* PSL Polysaccharide Is a Social but Noncheatable Trait in Biofilms. mBio
770 8:e00374-17.
- 771 41. Nadell CD, Drescher K, Foster KR. 2016. Spatial structure, cooperation and competition in biofilms. Nature
772 Reviews Microbiology 14:589-600.
- 773 42. Freschi L, Jeukens J, Kukavica-Ibrulj I, Boyle B, Dupont M-J, Laroche J, Larose S, Maaroufi H, Fothergill JL, Moore
774 M, Winsor GL, Aaron SD, Barbeau J, Bell SC, Burns JL, Camara M, Cantin A, Charette SJ, Dewar K, Déziel É,
775 Grimwood K, Hancock REW, Harrison JJ, Heeb S, Jelsbak L, Jia B, Kenna DT, Kidd TJ, Klockgether J, Lam JS, Lamont
776 IL, Lewenza S, Loman N, Malouin F, Manos J, McArthur AG, McKeown J, Milot J, Naghra H, Nguyen D, Pereira SK,
777 Perron GG, Pirnay J-P, Rainey PB, Rousseau S, Santos PM, Stephenson A, Taylor V, Turton JF, Waglechner N, et al.
778 2015. Clinical utilization of genomics data produced by the international *Pseudomonas aeruginosa* consortium.
779 Frontiers in Microbiology 6:1036.
- 780 43. De Soyza A, Hall AJ, Mahenthalingam E, Drevinek P, Kaca W, Drulis-Kawa Z, Stoitsova SR, Toth V, Coenye T,
781 Zlosnik JEA, Burns JL, Sá-Correia I, De Vos D, Pirnay J-P, J. Kidd T, Reid D, Manos J, Klockgether J, Wiehlmann L,
782 Tümmler B, McClean S, Winstanley C, pathogens" EfficACBCsvdocf. 2013. Developing an international
783 *Pseudomonas aeruginosa* reference panel. MicrobiologyOpen 2:1010-1023.
- 784 44. Cullen L, Weiser R, Olszak T, Maldonado RF, Moreira AS, Slachmuylders L, Brackman G, Paunova-Krasteva TS,
785 Zarnowiec P, Czerwonka G, Reilly J, Drevinek P, Kaca W, Melter O, De Soyza A, Perry A, Winstanley C, Stoitsova
786 SR, Lavigne R, Mahenthalingam E, Sá-Correia I, Coenye T, Drulis-Kawa Z, Augustyniak D, Valvano MA, McClean
787 S. 2015. Phenotypic characterization of an international *Pseudomonas aeruginosa* reference panel: strains of
788 cystic fibrosis (CF) origin show less in vivo virulence than non-CF strains. Microbiology 161:1961-1977.
- 789 45. Freschi L, Bertelli C, Jeukens J, Moore MP, Kukavica-Ibrulj I, Emond-Rheault J-G, Hamel J, Fothergill JL, Tucker NP,
790 McClean S, Klockgether J, de Soyza A, Brinkman FSL, Levesque RC, Winstanley C. 2018. Genomic characterisation
791 of an international *Pseudomonas aeruginosa* reference panel indicates that the two major groups draw upon
792 distinct mobile gene pools. FEMS Microbiology Letters 365.
- 793 46. Mischel W, Ebbesen EB, Raskoff Zeiss A. 1972. Cognitive and attentional mechanisms in delay of gratification.
794 Journal of Personality and Social Psychology 21:204-218.
- 795 47. Rahme LG, Stevens EJ, Wolfort SF, Shao J, Tompkins RG, Ausubel FM. 1995. Common virulence factors for
796 bacterial pathogenicity in plants and animals. Science 268:1899-1902.
- 797 48. Kuchma SL, Ballok AE, Merritt JH, Hammond JH, Lu W, Rabinowitz JD, O'Toole GA. 2010. Cyclic-di-GMP-mediated
798 repression of swarming motility by *Pseudomonas aeruginosa*: the *pilY1* gene and its impact on surface-
799 associated behaviors. J Bacteriol 192:2950-64.

- 800 49. de Anda J, Lee EY, Lee CK, Bennett RR, Ji X, Soltani S, Harrison MC, Baker AE, Luo Y, Chou T, O'Toole GA, Armani
801 AM, Golestanian R, Wong GCL. 2017. High-Speed "4D" Computational Microscopy of Bacterial Surface Motility.
802 ACS Nano 11:9340-9351.
- 803 50. O'Toole GA, Kolter R. 1998. Initiation of biofilm formation in *Pseudomonas fluorescens* WCS365 proceeds via
804 multiple, convergent signalling pathways: a genetic analysis. *Molecular Microbiology* 28:449-461.
- 805 51. O'Toole GA. 2011. Microtiter dish biofilm formation assay. *J Vis Exp* doi:10.3791/2437:e2437.
- 806 52. Holloway BW. 1955. Genetic Recombination in *Pseudomonas aeruginosa*. *Microbiology* 13:572-581.
- 807 53. Soare MV, Teodorescu PP, Toma I. 2007. Ordinary differential equations with applications to mechanics, vol 585.
808 Springer.
- 809 54. Khinchin AY, Andrews D, Quenouille MH. 2013. Mathematical methods in the theory of queuing. Courier
810 Corporation.
- 811 55. Gray J, Hancock GJ. 1955. The Propulsion of Sea-Urchin Spermatozoa. *J Exp Biol* 32:802-814.

812

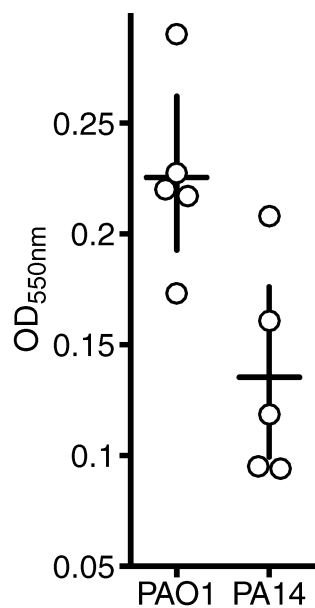
813 Supplementary Materials

814 Supplementary Figures



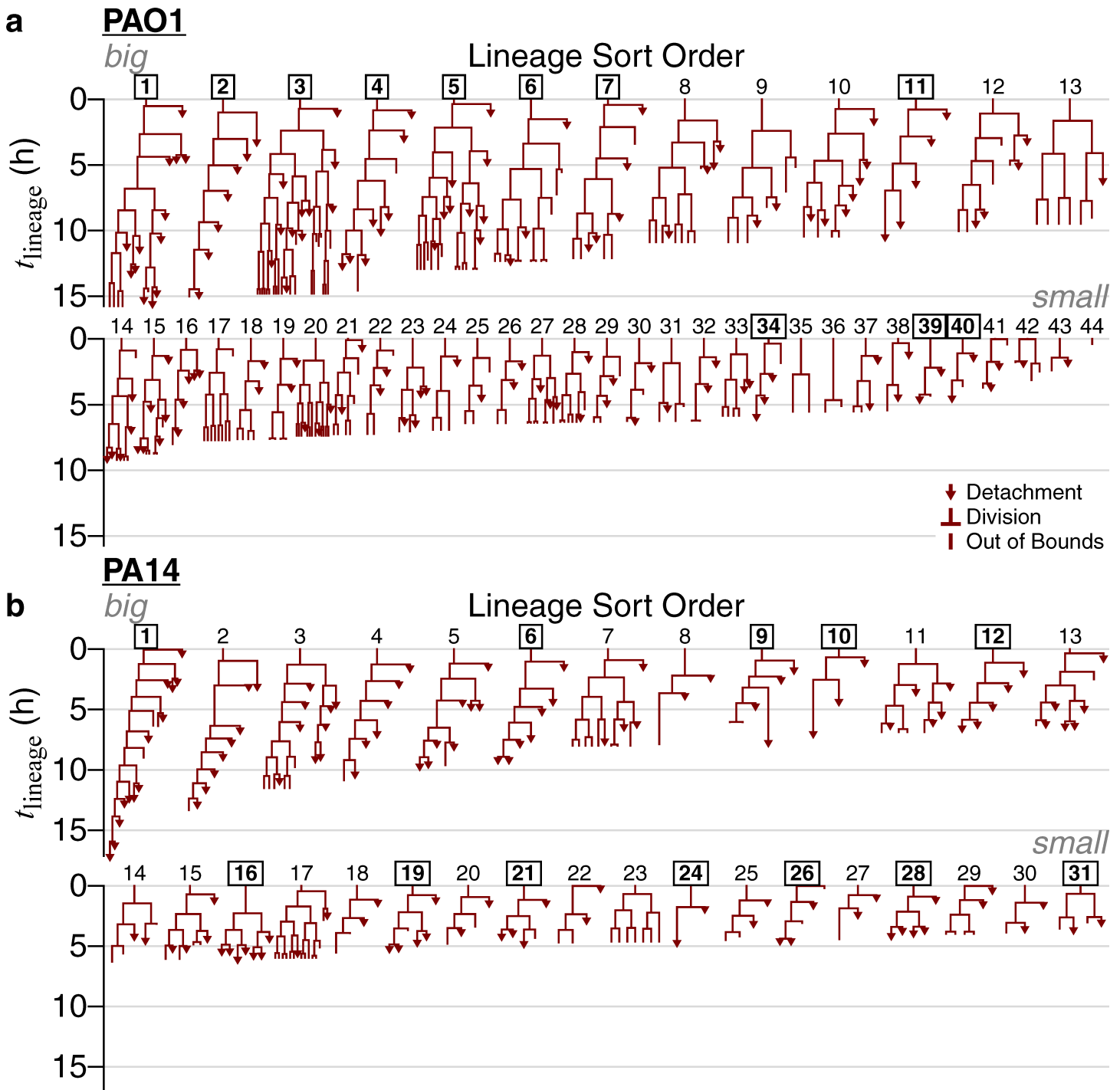
815

816 Figure S1. Exponential fits of bacteria count as a function of experiment time. (a) Each line is a fit to the function $N(t) =$
817 $N(0) \exp((t - t_{lag})/\tau_e)$ for data shown in Figure 1. $N(0)$ is the number of cells at time 0, t_{lag} characterizes the time
818 scale of the lag period where N is roughly constant, and τ_e characterizes the time scale of exponential increase ($1/\tau_e$
819 characterizes the rate of exponential increase). (b) Plots of τ_e vs. t_{lag} for the fits in part (a).



820

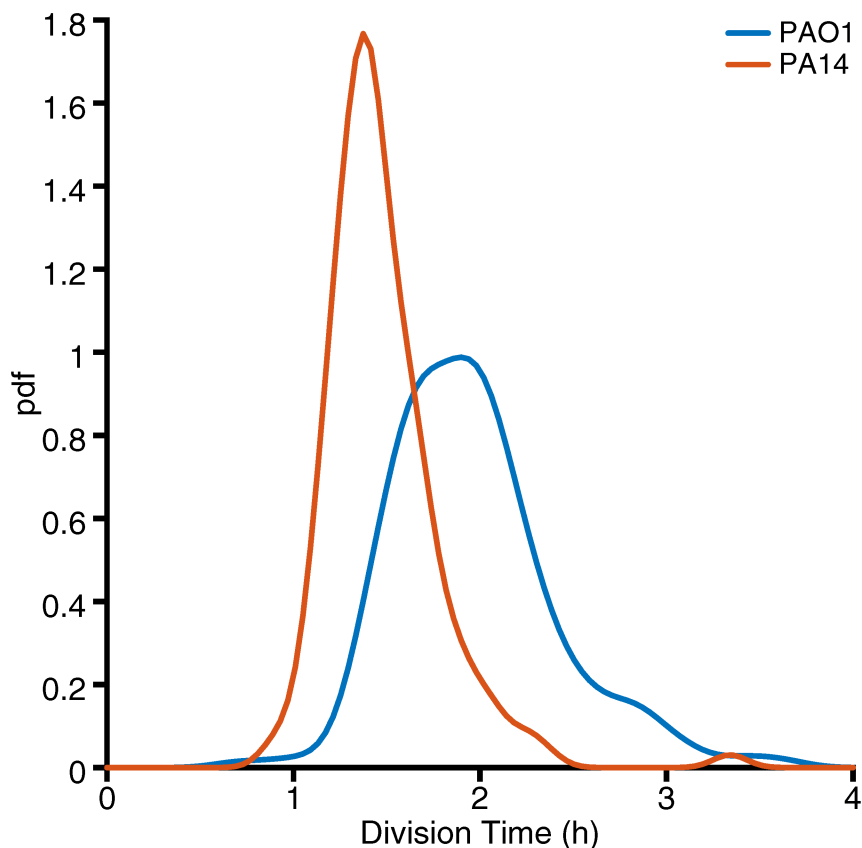
821 Figure S2. Monitoring biofilm formation via crystal violet assays. The OD_{550nm} values are proportional to the amount of
822 biofilm stained by crystal violet. Circles represent individual biological replicates, each of which is the mean of 4
823 technical replicates. Horizontal lines represent the mean OD_{550nm} values. Vertical lines indicate the 95% confidence
824 interval calculated from the bootstrap sampling distribution of the mean OD_{550nm} values.



825

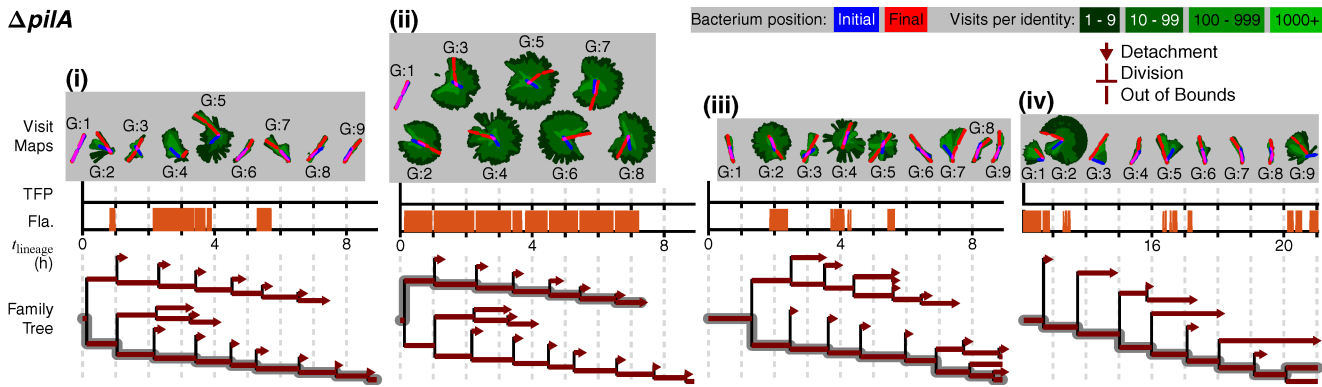
826 Figure S3. All families in the processive regime of reversible attachment, which is when cells divide at least once before
 827 detaching. We monitor the time that a given isolated family, consisting of an attached cell (founder cell) and its progeny
 828 (daughter cells), stays continually on the surface, which we designate as lineage time ($t = t_{\text{lineage}}$). For each family, we
 829 begin tracking at the frame individual, founder bacteria attach and assign this as $t_{\text{lineage}} = 0$ h. We continue tracking
 830 until either the entire family detaches, or until we lose track of that family (where we can no longer distinguish
 831 individual cells, or the cells move out of the recording boundaries). This final time point is recorded as the family's
 832 residence time. For families that we lose track of, their true residence times can be greater than or equal to these
 833 recorded values, while for families that end in detachment, their recorded and true residence times are equal. Only
 834 families that end in detachment are used for calculating the average residence time to avoid the uncertainty in actual
 835 residence times for families that we lose track of. For each regime and strain, we sort families by residence times in
 836 descending order, which sorts them by the amount of time that they have continuously contacted the surface. Lineage
 837 indices that are boxed and bolded are the families selected for use in the model. The criteria used to select families for
 838 the model are described as follows. We set the minimum number of families required for the model at ≈ 10 families.

839 First, we select all families that result in lineage “extinction” events (where we observe the family ending in a
840 detachment event), because these families all have defined outcomes (recorded and true residence times are equal).
841 Conversely, families that we lose track of (where we can no longer distinguish individual cells, or the cells move out of
842 the recording boundaries) have undefined outcomes (true residence times are greater than or equal to the recorded
843 residence times). For PA14, this results in 12 selected families (#1, 6, 9, 10, 12, 16, 19, 21, 24, 26, 28, and 31), which
844 meets the minimum family number requirement. For PAO1, this results in 4 selected families (#11, 34, 39, and 40), which
845 is not enough. To increase the number of selected families for PAO1, we apply a residence time cutoff on the families
846 with undefined outcomes, so that all selected families have defined outcomes at least in the lineage time window the
847 analysis is performed on. A residence time cutoff of $t_{\text{lineage}} = 12$ h results in an additional 7 families (#1-7) for a total of
848 11 selected families for PAO1, which meets the minimum family number requirement.



849

850 Figure S4. Distribution of division times for PAO1 and PA14. Division time is calculated as the time between
851 consecutively observed division events in a family. Distributions are plotted as pdf (probability density function)
852 calculated via kernel density estimation. PAO1 has a median division time of 1.92 h with a 95% confidence interval of
853 (1.87 h, 1.96 h), and PA14 has a median division time of 1.42 h with a 95% confidence interval of (1.38 h, 1.45 h). PAO1
854 has a mean \pm standard deviation division time of 1.96 ± 0.44 h, and PA14 has a mean \pm standard deviation division time
855 of 1.48 ± 0.30 h.



856

857

858

859

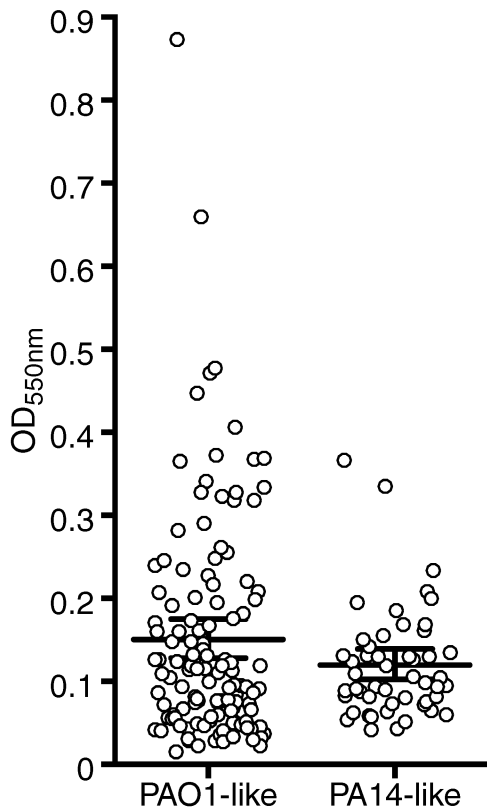
860

861

862

863

Figure S5. Appendage activity tracking for the $\Delta pilA$ mutant. We repeat the analysis in Figure 8 for the $\Delta pilA$ mutant and find one predominant behavior up the 9 generations shown here, consistent with this strain having predominantly one-legged division branching (8). We observe no TFP activity, which is consistent with this strain having no TFP; we observe sporadic, but prolonged, flagellum activity, which is consistent with observations of this strain spinning on the surface for prolonged periods of time; and we observe detachment events without flagellum activity, which is consistent with observations of detachment events where cells did not have a labeled flagellum. Beyond generation 9, the $\Delta pilA$ mutant continues to have mainly one-legged division-branching for multiple subsequent generations.



864

865

866

867

868

869

870

871

872

Figure S6. Crystal violet biofilm assay results for 35 *P. aeruginosa* strains (25 PAO1-like and 10 PA14-like strains, including PAO1 and PA14 strains) in the International *P. aeruginosa* Consortium Database (IPCD). These strains are identified as either PAO1-like or PA14-like based on their phylogeny (i.e., same phylogenetic sub-group as either PAO1 or PA14) (42-45). The OD_{550nm} values are proportional to the amount of biofilm stained by crystal violet. Circles represent individual biological replicates, each of which is the mean of 4 technical replicates. Longer horizontal lines represent the mean OD_{550nm} values. Vertical lines and error bars indicate the 95% confidence interval calculated from the bootstrap sampling distribution of the mean OD_{550nm} values. Comparing these distributions shows that the mean OD_{550nm} value for the PAO1-like strains are higher than the mean OD_{550nm} value for PA14-like strains (p-value of 0.02).

873

874 Tables

875 Table S1. Strains used in the crystal violet biofilm assays. The collection of isolates was described in (43). (CF = cystic
876 fibrosis)

Strain ID	Source ID	Local Strain collection #	Origin and source	Original reference
PA14 WT		DH123	PA14 <i>P. aeruginosa</i> wild type	(47)
PAO1 WT		DH1467	PAO1 <i>P. aeruginosa</i> wild type	(56)
1268	15108-1	DH3446	ICU (acute infection), Spain	(57)
87	679	DH3418	Non CF Urine sample, male, Wroclaw Poland, 2011	(43)
95	CPHL9433	DH3425	Tobacco plant, Philippines	(58)
1103	AUS23	DH3436	Adult CF (2007), Brisbane, Australia	(59)
80	AMT0060-1	DH3411	Pediatric CF, Seattle, WA	(60)
1273	TBCF10839	DH3451	CF, Germany	(61)
1260	AMT0023-30	DH3441	Pediatric CF, Seattle, WA	(60)
94	U018A	DH3424	Hobart, Australia, CF patient	(58)
92	LMG14084	DH3422	Bucharest, Romania, Water, 1960-1964	(58)
85	IST27N	DH3416	Lisbon Portugal, CF patient	(62)
1259	AA2	DH3440		
93	Pr335	DH3423	Prague, Czech Republic, Hospital environment 1997	(58)
91	Jpn1563	DH3421	Lake Tamaco, Japan, Lake water, 2003	(58)
84	IST27	DH3415	Lisbon Portugal, CF patient	(62)
1258	AUS52	DH3439	Adult CF (2008), Hobart, Australia	(63, 64)
1266	Mi162-2	DH3445	Non CF burn, Ann Arbor, MI, 1997	(58)
89	1709-12	DH3420	Leuven Belgium Non CF clinical 2004	(58)
2495	LES400	DH3459	CF, U.K.	(65)
1272	A5803	DH3450	Community-acquired pneumonia	(66)
1264	39016	DH3444	Keratitis eye isolate, U.K.	(67)
88	NH57388A	DH3419	CF, Denmark	(68)
2496	LES431	DH3460	Non CF parent of CF patient, U.K.	(67)
1271	KKI	DH3449	CF, Germany	(69)
1262	CHA	DH3443	CF	(70)
83	PAK	DH3414	Clinical non CF	(71)
2617	LESB58	DH3461	CF, U.K., 1988	(72)
1270	39177	DH3448	Keratitis, Manchester U.K.	(67)
1261	AMT0023-34	DH3442	Pediatric CF, Seattle, WA	(60)

Strain ID	Source ID	Local Strain collection #	Origin and source	Original reference
82	AMT0060-3	DH3413	Pediatric CF, Seattle, WA	(60)
2045	UCBPP-PA14	DH3458	Human Burn isolate	(47)
1269	13121-1	DH3447	ICU (acute infection), France	(66)
1256	C3719	DH3437	CF, Manchester, U.K.	(73)
81	AMT0060-2	DH3412	Pediatric CF, Seattle, WA	(60)

877

878 Supplementary References

- 879 8. Lee CK, de Anda J, Baker AE, Bennett RR, Luo Y, Lee EY, Keefe JA, Helali JS, Ma J, Zhao K, Golestanian R, O'Toole
880 GA, Wong GCL. 2018. Multigenerational memory and adaptive adhesion in early bacterial biofilm communities.
881 *Proceedings of the National Academy of Sciences* 115:4471-4476.
- 882 42. Freschi L, Jeukens J, Kukavica-Ibrulj I, Boyle B, Dupont M-J, Laroche J, Larose S, Maaroufi H, Fothergill JL, Moore
883 M, Winsor GL, Aaron SD, Barbeau J, Bell SC, Burns JL, Camara M, Cantin A, Charette SJ, Dewar K, Déziel É,
884 Grimwood K, Hancock REW, Harrison JJ, Heeb S, Jelsbak L, Jia B, Kenna DT, Kidd TJ, Klockgether J, Lam JS, Lamont
885 IL, Lewenza S, Loman N, Malouin F, Manos J, McArthur AG, McKeown J, Milot J, Naghra H, Nguyen D, Pereira SK,
886 Perron GG, Pirnay J-P, Rainey PB, Rousseau S, Santos PM, Stephenson A, Taylor V, Turton JF, Waglechner N, et al.
887 2015. Clinical utilization of genomics data produced by the international *Pseudomonas aeruginosa* consortium.
888 *Frontiers in Microbiology* 6:1036.
- 889 43. De Soyza A, Hall AJ, Mahenthalingam E, Drevinek P, Kaca W, Drulis-Kawa Z, Stoitsova SR, Toth V, Coenye T,
890 Zlosnik JEA, Burns JL, Sá-Correia I, De Vos D, Pirnay J-P, J. Kidd T, Reid D, Manos J, Klockgether J, Wiehlmann L,
891 Tümmler B, McClean S, Winstanley C, pathogens" EFCABCsvdocf. 2013. Developing an international
892 *Pseudomonas aeruginosa* reference panel. *MicrobiologyOpen* 2:1010-1023.
- 893 44. Cullen L, Weiser R, Olszak T, Maldonado RF, Moreira AS, Slachmuylders L, Brackman G, Paunova-Krasteva TS,
894 Zarnowiec P, Czerwonka G, Reilly J, Drevinek P, Kaca W, Melter O, De Soyza A, Perry A, Winstanley C, Stoitsova
895 SR, Lavigne R, Mahenthalingam E, Sá-Correia I, Coenye T, Drulis-Kawa Z, Augustyniak D, Valvano MA, McClean
896 S. 2015. Phenotypic characterization of an international *Pseudomonas aeruginosa* reference panel: strains of
897 cystic fibrosis (CF) origin show less in vivo virulence than non-CF strains. *Microbiology* 161:1961-1977.
- 898 45. Freschi L, Bertelli C, Jeukens J, Moore MP, Kukavica-Ibrulj I, Emond-Rheault J-G, Hamel J, Fothergill JL, Tucker NP,
899 McClean S, Klockgether J, de Soyza A, Brinkman FSL, Levesque RC, Winstanley C. 2018. Genomic characterisation
900 of an international *Pseudomonas aeruginosa* reference panel indicates that the two major groups draw upon
901 distinct mobile gene pools. *FEMS Microbiology Letters* 365.
- 902 47. Rahme LG, Stevens EJ, Wolfort SF, Shao J, Tompkins RG, Ausubel FM. 1995. Common virulence factors for
903 bacterial pathogenicity in plants and animals. *Science* 268:1899-1902.
- 904 56. Stover CK, Pham XQ, Erwin AL, Mizoguchi SD, Warrenner P, Hickey MJ, Brinkman FS, Hufnagle WO, Kowalik DJ,
905 Lagrou M, Garber RL, Goltry L, Tolentino E, Westbrook-Wadman S, Yuan Y, Brody LL, Coulter SN, Folger KR, Kas A,
906 Larbig K, Lim R, Smith K, Spencer D, Wong GK, Wu Z, Paulsen IT, Reizer J, Saier MH, Hancock RE, Lory S, Olson
907 MV. 2000. Complete genome sequence of *Pseudomonas aeruginosa* PAO1, an opportunistic pathogen. *Nature*
908 406:959-964.
- 909 57. Köhler T, Buckling A, van Delden C. 2009. Cooperation and virulence of clinical *Pseudomonas aeruginosa*
910 populations. *Proceedings of the National Academy of Sciences* 106:6339-6344.
- 911 58. Pirnay J-P, Bilocq F, Pot B, Cornelis P, Zizi M, Van Eldere J, Deschaght P, Vaneechoutte M, Jennes S, Pitt T, De Vos
912 D. 2009. *Pseudomonas aeruginosa* Population Structure Revisited. *PLOS ONE* 4:e7740.
- 913 59. O'Carroll MR, Szymis MW, Wainwright CE, Greer RM, Mitchell P, Coulter C, Sloots TP, Nissen MD, Bell SC. 2004.
914 Clonal strains of *Pseudomonas aeruginosa* in paediatric and adult cystic fibrosis units. *European Respiratory*
915 *Journal* 24:101-106.
- 916 60. Mulcahy LR, Burns JL, Lory S, Lewis K. 2010. Emergence of *Pseudomonas aeruginosa* Strains Producing High
917 Levels of Persister Cells in Patients with Cystic Fibrosis. *Journal of Bacteriology* 192:6191-6199.
- 918 61. Bezuidt OK, Klockgether J, Elsen S, Attree I, Davenport CF, Tümmler B. 2013. Intraclonal genome diversity of
919 *Pseudomonas aeruginosa* clones CHA and TB. *BMC Genomics* 14:416.
- 920 62. Leitão JH, Alvim T, Sá-Correia I. 1996. Ribotyping of *Pseudomonas aeruginosa* isolates from patients and water
921 springs and genome fingerprinting of variants concerning mucoidy. *Pathogens and Disease* 13:287-292.
- 922 63. Bradbury R, Champion A, Reid DW. 2008. Poor clinical outcomes associated with a multi-drug resistant clonal
923 strain of *Pseudomonas aeruginosa* in the Tasmanian cystic fibrosis population. *Respirology* 13:886-892.
- 924 64. Kidd TJ, Ramsay KA, Hu H, Marks GB, Wainwright CE, Bye PT, Elkins MR, Robinson PJ, Rose BR, Wilson JW,
925 Grimwood K, Bell SC. 2013. Shared *Pseudomonas aeruginosa* genotypes are common in Australian cystic fibrosis
926 centres. *European Respiratory Journal* 41:1091-1100.
- 927 65. Salunkhe P, Smart CHM, Morgan JAW, Panagea S, Walshaw MJ, Hart CA, Geffers R, Tümmler B, Winstanley C.
928 2005. A Cystic Fibrosis Epidemic Strain of *Pseudomonas aeruginosa* Displays Enhanced Virulence and
929 Antimicrobial Resistance. *Journal of Bacteriology* 187:4908-4920.

- 930 66. Wiehlmann L, Wagner G, Cramer N, Siebert B, Gudowius P, Morales G, Köhler T, van Delden C, Weinel C, Slickers
931 P, Tümmler B. 2007. Population structure of *Pseudomonas aeruginosa*. Proceedings of the National Academy of
932 Sciences 104:8101-8106.
- 933 67. Stewart RMK, Wiehlmann L, Ashelford KE, Preston SJ, Frimmersdorf E, Campbell BJ, Neal TJ, Hall N, Tuft S, Kaye
934 SB, Winstanley C. 2011. Genetic Characterization Indicates that a Specific Subpopulation of *Pseudomonas*
935 *aeruginosa* Is Associated with Keratitis Infections. Journal of Clinical Microbiology 49:993-1003.
- 936 68. Hoffmann N, Rasmussen TB, Jensen P, Stub C, Hentzer M, Molin S, Ciofu O, Givskov M, Johansen HK, Høiby N.
937 2005. Novel Mouse Model of Chronic *Pseudomonas aeruginosa* Lung Infection Mimicking Cystic Fibrosis.
938 Infection and Immunity 73:2504-2514.
- 939 69. Cramer N, Wiehlmann L, Ciofu O, Tamm S, Høiby N, Tümmler B. 2012. Molecular Epidemiology of Chronic
940 *Pseudomonas aeruginosa* Airway Infections in Cystic Fibrosis. PLOS ONE 7:e50731.
- 941 70. Toussaint B, Delicattree I, Vignais PM. 1993. *Pseudomonas aeruginosa* Contains an IHF-like Protein That Binds to
942 the *algD* Promoter. Biochemical and Biophysical Research Communications 196:416-421.
- 943 71. Totten PA, Lory S. 1990. Characterization of the type a flagellin gene from *Pseudomonas aeruginosa* PAK. Journal
944 of Bacteriology 172:7188-7199.
- 945 72. Kukavica-Ibrulj I, Bragonzi A, Paroni M, Winstanley C, Sanschagrin F, O'Toole GA, Levesque RC. 2008. In Vivo
946 Growth of *Pseudomonas aeruginosa* Strains PAO1 and PA14 and the Hypervirulent Strain LESB58 in a Rat Model
947 of Chronic Lung Infection. Journal of Bacteriology 190:2804-2813.
- 948 73. Jones AM, Dodd ME, Doherty CJ, Govan JR, Webb AK. 2002. Increased treatment requirements of patients with
949 cystic fibrosis who harbour a highly transmissible strain of *Pseudomonas aeruginosa*. Thorax 57:924-925.

950